A COMPUTER SIMULATION OF REACTION PLANE MEMORY VIA QUASIPARTICLE DYNAMICS

by

John Chun Kit Wong

B.Sc. (Hons.), Simon Fraser University, 1985.

THESIS SUBMITTED IN PARTIAL FULFILLMENT OF

THE REQUIREMENTS FOR THE DEGREE OF

MASTER OF SCIENCE

in the Department

of

PHYSICS

SIMON FRASER UNIVERSITY

January, 1990

APPROVAL

Name: John Chun Kit Wong

Degree: M.Sc. (Physics)

Title of Thesis: A Computer Simulation of Reaction Plane Memory via Quasiparticle Dynamics.

Examining Committee:

Chairman: E.D. Crozier

D.H. Boal
Professor
Senior Supervisor

R.G. Korteling
Professor
Department of Chemistry

K.S. Viswanathan
Professor

R.M. Woloshyn
Adjunct Professor
External Examiner

PARTIAL COPYRIGHT LICENSE

I hereby grant to Simon Fraser University the right to lend my thesis, project or extended essay (the title of which is shown below) to users of the Simon Fraser University Library, and to make partial or single copies only for such users or in response to a request from the library of any other university, or other educational institution, on its own behalf or for one of its users. I further agree that permission for multiple copying of this work for scholarly purposes may be granted by me or the Dean of Graduate Studies. It is understood that copying or publication of this work for financial gain shall not be allowed without my written permission.

Title of Thesis/Project/Extended Essay

A Computer Simulation of Reaction Plane Memory via Quasiparticle Dynamics.

Author: _____
(signature)

John Chun Kit Wong
(name)

Mar. 5, 1990
(date)

ABSTRACT

Quasiparticle Dynamics, a computer simulation for nuclear reactions, is used to investigate reaction plane memory in intermediate energy heavy ion collisions. In particular, extensive simulations involving the generation of more than 21,000 events are performed for $^{14}N+^{154}Sm$ at 35 A.MeV. The gamma ray circular polarization, as a function of trigger mass, energy and angle, is shown to be a measure of the correlation between the trigger plane and the reaction plane. Calculations of the inclusive particle spectrum, as well as circular polarization, are compared with experiment and the Boltzmann-Uehling-Uhlenbeck model. The dependence of the calculated observables on the assumed in-medium nucleon-nucleon cross section is also investigated.

ACKNOWLEDGEMENTS

I would like to thank my supervisor David Boal for giving me the problem to work on and for guiding me all the way. I must express my gratitude to the Natural Sciences and Engineering Research Council of Canada and the Department of Physics for financial support.

TABLE OF CONTENTS

LIST OF TABLES

LIST OF FIGURES

Chapter One

Introduction

1.1 Introduction

In heavy ion collisions, nuclear matter is usually compressed at the early stage of the reaction because of the interpenetration of the projectile and the target. Nucleon-nucleon collisions cause both the temperature and the entropy of the system to rise. The state of compression can only last for a very short time, typically about 30 fm/c=10^{-22} second. Then the system disassembles. The number of nucleon-nucleon collisions falls quickly and the entropy changes slowly. During the expansion phase of the reaction, the density decreases to a value where the nucleons are no longer interacting. This density is called the freeze-out density. In heavy ion reaction experiments, the detectors can only measure the experimental observables long after this stage. To understand the whole process of a nuclear reaction requires detailed analysis of the experimental observables. Reviews of heavy ion collision phenomena can be found in References 1 to 3.

Computer simulations have been used for more than a quarter of a century to study some aspects of nuclear physics.[4] In nuclear reaction experiments, the observables such as momenta and energies of particles emitted are measured a long time after the reaction begins. One cannot understand the step-by-step mechanism of the

reaction from the measured observables alone. The advantage of computer simulation is that one can study the reaction at any time step throughout the whole reaction process. Further, experiments have no control on either the magnitude or the direction of the impact parameter between the projectile and the target in heavy ion reactions. In a computer simulation, the impact parameter can be set at whatever value desired.

In many heavy ion collisions, the number of nucleons involved will be in the order of 100 and the reaction cannot be easily described in analytical form. The fermionic nature of nucleons requires that the antisymmetric wave function of a nucleus will have at least A! terms. There will be many more terms if one wants to determine the expectation value of observables such as kinetic energy. It would be computationally demanding to determine the time evolution problem of any observable by numerically propagating the nuclear wave function except for very light nuclei. Many models have been developed to attempt to reduce the many-body problem to a computationally manageable scale. In the next section, a brief review of computer simulations in nuclear studies is discussed.

1.2 Brief Review of Computer Simulations In Nuclear Reaction Studies

Several different models have been developed in the history of computer simulation of heavy ion collisions. One of the earliest methods of simulating nuclear reactions is by modelling the reaction

using the equations of hydrodynamics. If the mean free path of a nucleon in nuclear matter is sufficiently short, then a local equilibrium may be established within the reaction zone and the region may evolve according to hydrodynamics. The nucleon mean free path is estimated to be of the order of the internucleon spacing.[5] One can determine the trajectory of a nuclear reaction by solving the hydrodynamic equations governing the time evolution of quantities such as the energy density, number density and momentum density.[6] The attraction of hydrodynamics is the simplicity of its ingredients: conservation laws and an equation of state. Several numerical solutions of the hydrodynamic equations for heavy ion collisions have been performed.[6] However, hydrodynamics demands that individual nucleon-nucleon collisions are frequent enough to maintain a local equilibrium during the course of a reaction. This method is not applicable to intermediate energy heavy ion collision.

A more exclusive model than hydrodynamics is the Intranuclear Cascade Model (INC) in which nucleons are propagated in space by means of classical mechanics.[7] The motion of the nucleons is a straight line unless it is affected by a nucleon-nucleon collision, which occurs if the distance of closest approach of two nucleons falls below the classical scattering radius determined by the measured nucleon-nucleon (NN) cross section. This model is computationally fast and simple. Furthermore, it is a true A-body problem. It has been used to address a number of questions about the internal dynamics of a reaction such as the production of entropy in central collisions.[8] However, neither the nuclear potential nor the Pauli

Exclusion Principle are considered in this model, and it cannot be used to describe fragment formation in nuclear reactions.

For reactions at low energy, i.e., the projectile kinetic energy per nucleon is a few MeV above the Coulomb barrier, many of the individual nucleon-nucleon collisions are Pauli-blocked. The reaction is dominated by the nuclear mean field. Nucleus-nucleus collisions at small impact parameter lead to complete fusion of the projectile and the target. An equilibrated compound nucleus is formed. The deexcitation of the compound nucleus is by emission of particles and photons. At large impact parameters, the collisions are dominated by quasi-elastic reactions. At intermediate impact parameter collisions, the two nuclei largely retain their form but there is a large momentum and energy transfer.[2]

Some aspects of the nuclear reactions at low energy can be described by the Vlasov equation[9] which is the Boltzmann equation without the collision term:

$$\frac{\partial f}{\partial t} + \mathbf{v}\cdot\frac{\partial f}{\partial \mathbf{r}} - \nabla U\cdot\frac{\partial f}{\partial \mathbf{p}} = 0 \qquad (1.1)$$

where f(r,p,t) is the one-body phase space density and U is the nuclear potential function. However, since it neglects nucleon-nucleon collisions, the Vlasov equation cannot be used to describe reactions at higher energies.

For intermediate energy reactions, the projectile kinetic energy per nucleon is in the range of 20 to 200 MeV. The relative velocity of

the two colliding nuclei in this range of energies is comparable in magnitude to the Fermi velocity in nuclear matter, $v_F \approx 0.3c$.

In intermediate energy nuclear reaction, the energy is not high enough that the nuclear mean field and the Pauli exclusion principle can be neglected nor is it low enough that most of nucleon-nucleon collisions can be ignored because of Pauli blocking factor.

1.3 Boltzmann-Uehling-Uhlenbeck Equation

One way of addressing the intermediate energy nuclear reaction problem is by solving the Boltzmann equation for the single particle phase space distribution $f(r,p,t)$. The equation includes both a force term, given by the gradient of the mean field potential, and also a collision integral term. However, this method is not very appropriate because effects such as Pauli blocking arising from nucleon-nucleon collisions are excluded. Therefore the nucleon-nucleon collision term should include the Pauli blocking factor for fermions as suggested by Nordheim[10] and Uehling and Uhlenbeck.[11] An equation resembling the classical Boltzmann equation has been developed for fermion distributions and is known as the Boltzmann-Uehling-Uhlenbeck (BUU) equation:

$$\frac{\partial f}{\partial t} + \mathbf{v}\cdot\frac{\partial f}{\partial \mathbf{r}} - \nabla U\cdot\frac{\partial f}{\partial \mathbf{p}} = -\int \frac{d^3p_2\, d^3p'_1\, d^3p'_2}{(2\pi)^6} v_{12}\, \sigma(\mathbf{p}+\mathbf{p}_2\rightarrow\mathbf{p}'_1+\mathbf{p}'_2)$$

$$\times [ff_2(1-f_1')(1-f_2')-f_1'f_2'(1-f)(1-f_2)]\ \delta^3(p_1+p_2-p'_1-p'_2) \qquad (1.2)$$

The right hand side of equation (1.2) is the collision integral. The effects of the Pauli exclusion principle are partly included in the collision term: the $(1-f)(1-f)$ terms inhibit nucleon scattering into regions of high density in phase space. If the right hand side is equal to zero, the equation reduces to the Vlasov equation (1.1). Solutions of equation (1.2) are usually found by using the Monte Carlo sampling technique.[12] We will briefly discuss the numerical techniques for the BUU model in the next chapter.

In many BUU calculations, the initialization used to represent the "ground state nucleus" is numerically unstable on the time scale of a few hundred fm/c. The initialization is not the true ground state of the potential U. Particles are slowly evaporated from a 'cold' nucleus even if there is no nuclear reaction. Therefore the calculation has to stop at about 200 fm/c in order to avoid evaporation of the system.[13]

The BUU-like models are widely applied in intermediate and high energy nuclear reactions. For example, it has been used to calculate the proton spectra observed in the $^{12}C+^{16}O$ reaction at 25 A.MeV.[14] Its predictions are in good agreement with the experiment. The BUU model which includes nucleon-nucleon collisions gives better

predictions for intermediate energy heavy ion reactions than the Vlasov equation. For example, a comparison between the Vlasov and the BUU equations of the momentum space distribution for a central Ar+Ca collision at 137 A.MeV has been made.[15] In the Vlasov approach, the final momentum distribution is still fairly close to that of the initial projectile and target, i.e., the nuclei are largely transparent to each other. On the other hand, the BUU approach shows a much larger change of the momentum distribution, and is in closer agreement with experiment. Discussion about the applications of the BUU model can be found in review articles Refs. 1-4.

1.4 Quasiparticle Dynamics

The BUU model is a one-body model. The correlations between nucleons have to be incorporated in a model-dependent fashion. For example, a number of assumptions must be made in order to extract fragments from the one-body distribution (we will discuss these aspects in Chapter Three.)

In the time since the BUU model was developed, a considerable amount of effort[16] has gone into developing simulations for many-particle distributions. These simulations include correlations between nucleons and so incorporate fragment emission from heavy ion reactions without further assumptions. One such model is the Quasiparticle Dynamics model,[17] which is Hamiltonian-based yet includes a stochastic nucleon-nucleon collision term.

In the Quasiparticle Dynamics model, each nucleon is represented by a Gaussian wavepacket of width $1/\alpha$ in coordinate space. The degrees of freedom for the equations of motion are taken to be $\langle x \rangle$ and $\langle p \rangle$, the expectations of the individual wavepackets. Hence, each nucleon is represented by a quasiparticle whose phase space coordinates **R** and **P** are $\langle x \rangle$ and $\langle p \rangle$ respectively.

The wavepackets are not used to form an antisymmetric wavefunction but a momentum-dependent potential acting pairwise between the quasiparticles is used to incorporate many of the effects on the fermions' energies arising from antisymmetrization. The complete Hamiltonian of the system also includes terms representing the nuclear interaction and the coulomb interaction. In Chapter Two, we give a brief description of the development of the QPD model.

In Chapter Three, we use the Quasiparticle Dynamics (QPD) model to simulate the reaction $^{14}N+^{154}Sm$ at 35 A.MeV. The properties of the residual nuclei and the single particle spectra are studied. The predicted spectra are compared with experiment and results from a BUU calculation.

1.5 Gamma Ray Circular Polarization

One of the features of intermediate energy nuclear reactions is the incomplete fusion reaction. By definition, complete fusion reactions involve the projectile and the target completely fusing together and the momentum of the projectile being transferred to the composite

system. The life-time of the compound nucleus is long enough that the internal degrees of freedom are equilibrated and memory of the entrance channel is lost. Particles are emitted by evaporation and their distribution is isotropic in the nucleus-nucleus center-of-mass frame. The velocity distribution of the residual nuclei is centered about the center-of-mass of the system.

Incomplete fusion reactions denote processes in which some particles are emitted prior to the complete equilibration of the composite system. Those particles are called nonequilibrium particles, and are more energetic than those evaporated from the equilibrated nucleus. The angular distributions of the emitted particles are usually not isotropic in the center-of-mass frame. In the laboratory frame, the nonequilibrium light particle spectra are forward peaked. (See, for example, data summarized in Refs. 1-3.)

Experimental evidence[18] indicates that nonequilibrium particle emission in an incomplete fusion reaction exhibits preferential emission in the reaction plane which is perpendicular to the orbital angular momentum, $\mathbf{J}_i$, of relative motion between projectile and target nuclei. The reaction plane is defined by the impact parameter vector, $\mathbf{b}$, and momentum vector of the beam, $\mathbf{k}_i$, where $\mathbf{J}_i$ is defined as $\mathbf{b}\times\mathbf{k}_i$. Tsang and co-workers detected light particles in coincidence with two binary fission fragments for ^{14}N induced reactions on ^{197}Au at 30 A.MeV incident kinetic energy.[18] The two detected coincident fission fragments and the beam form the fission plane which is perpendicular to the orbital momentum of the fissioning nucleus. For simplicity, the intrinsic spins of the projectile and target nuclei and

the angular momentum of particles emitted prior to fission are neglected. In this approximation, the total angular momentum of the fissioning nucleus is equal to the orbital angular momentum of relative motion between projectile and target nuclei. Therefore, the fission plane is approximately coplanar with the reaction plane. The light particles detected in the fission plane are called 'in-plane' particles while those detected perpendicular to the fission plane are called 'out-of-plane' particles. The ratio of particles emitted out-of-plane to those emitted in-plane is less than one. Thus the experiment shows preferential emission of light particles in the reaction plane.

Preferential emission of nonequilibrium light particles is observed in the reaction plane, indicating a collective motion in this plane and transverse to the beam axis. To discuss this question quantitatively, let us define a sign convention for the reaction plane and angle. Figure 1 shows the sign of the deflection angle for emission of light particles. The quantization axis is defined as $\hat{\mathbf{n}}_{if}=\frac{\mathbf{k}_i\times\mathbf{k}_f}{|\mathbf{k}_i\times\mathbf{k}_f|}$. Thus, negative (positive) deflection angles of emission correspond to $\hat{\mathbf{n}}_{if}\cdot\mathbf{J}_i$ being positive (negative).

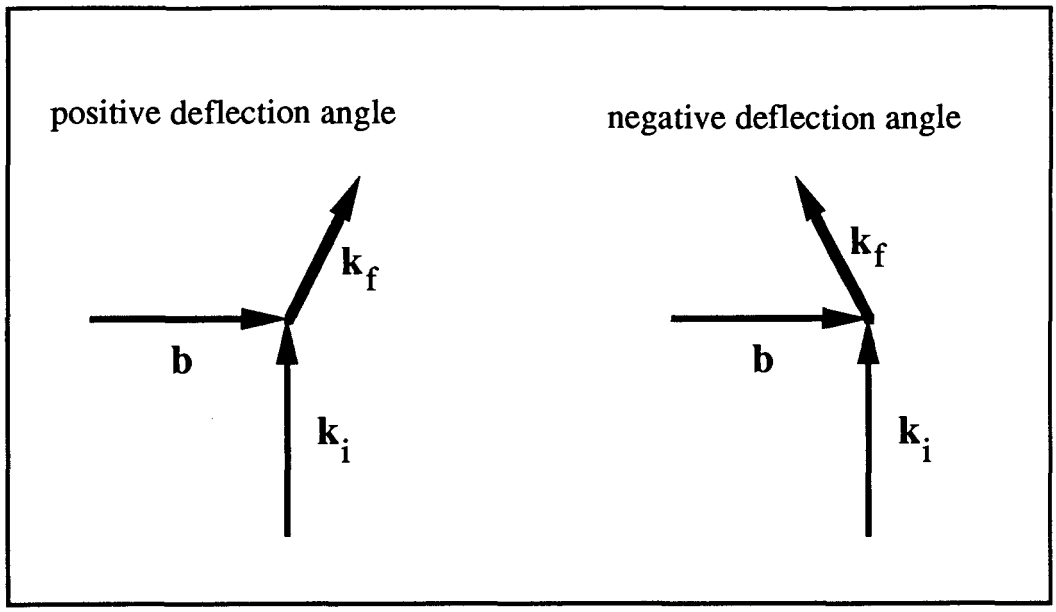

Fig. 1.1 Sign convention for the deflection angles of the particles emitted. The momentum vector of the beam and that of the light particles are defined as $\mathbf{k}_i$ and $\mathbf{k}_f$ respectively. The impact parameter vector is defined as $\mathbf{b}$.

Microscopic calculations[14] with the Boltzmann-Uehling-Uhlenbeck equation interpret the effects of enhanced emission of nonequilibrium light particles in the reaction plane (at intermediate bombarding energies) in terms of the deflection to negative emission angles by the attractive nuclear mean field. Since collective motion in the mean field is damped by the individual nucleon-nucleon collisions, the relative importance of positive and negative emission angles is sensitive to the interplay between mean-field dynamics and two-body dissipation.

To address this issue, Tsang and co-workers[19] measured the circular polarization of gamma-rays emitted by the residual nucleus in

coincidence with nonequilibrium light particle triggers for the reaction ^{14}N on ^{154}Sm. The triggers are measured at polar angles of 30° and 60° with respect to the beam. The photons are detected around the quantization axis. The sign of the gamma ray circular polarization follows the sign of the average emission angle of nonequilibrium light particles. Since light particles are preferentially emitted in the reaction plane, the quantization axis will be aligned with the angular momentum, **J**, of the heavy residue. Semiclassically, the photon's spin will be parallel to the spin of the residue. Therefore, positive circular polarization corresponds to negative deflection and an attractive mean field.

Positive circular polarizations are observed for all light particle triggers at both angles. The magnitude of the measured polarization increases with increasing energy and mass of the triggers. This experiment establishes the preferential emission of nonequilibrium light particles to negative emission angles, consistent with an attractive nuclear mean field calculated by the BUU model and with measurements at lower energies.[20]

In Chapter Four, we use the QPD model to calculate the sign and the magnitude of the gamma ray circular polarization in coincidence with the light particle triggers. The results are compared with experiment and the BUU code. We also study the microscopic dynamics of the nucleus-nucleus collision process. Finally, our conclusions and discussion are included in Chapter Five.

Chapter Two

Quasiparticle Dynamics

2.1 Introduction

On a quantum mechanical level, the fermionic nature of nucleons demands that a nuclear wave function has to be antisymmetrized. Thus there will be A! components to the wave function for a single Slater determinant of a single nucleus of A nucleons. For all but the lightest nuclei, it is impossible for existing computers to handle any time evolution problem in nuclear reactions by propagating the nuclear wave functions. Thus it is difficult to find a model to describe nuclei in an efficient manner in computer simulations.

One method of tackling the problem is to find a classical potential which can incorporate some of the effects of antisymmetrization. In the Quasiparticle Dynamics (QPD) model,[17] the classical potential (referred to as the Pauli potential) is obtained from evaluating the expectation value of the kinetic-energy operator for a specific nuclear wave function. Then the nuclear and Coulomb terms are added to the potential such that the Hamiltonian of the system involves A^2 terms. With this simplification, systems with several hundred nucleons can be investigated by computer simulation.

The layout of this chapter is as follows: In Section 2.2 the derivation of the Pauli potential in QPD is described. The properties of ground

state nuclei in QPD are discussed in Section 2.3. In Section 2.4 the nucleon-nucleon collision term is discussed. Finally, the differences between BUU and QPD are compared in Section 2.5.

2.2 Pauli Potential

One of the effects of Fermi-Dirac statistics is that the ground state of a fermion system has to have a non-zero expectation value of the kinetic energy operator:

$$\langle \hat{K} \rangle = \frac{-\hbar^2}{2m} \left\langle \Psi_{g.s.} \mid \sum_i \nabla_i^2 \mid \Psi_{g.s} \right\rangle . \qquad (2.1)$$

where the mass of the nucleon, m, is assigned to be 938.9 MeV. One can see that there are at least $A(A!)^2$ terms in equation (2.1) for a nucleus with A nucleons, if $\Psi_{g.s.}$ is antisymmetric. It is computationally prohibitive to propagate equation (2.1) for all but light nuclei. The motivation for the Quasiparticle Dynamics model is to try to seek approximations to express equation (2.1) in terms of a two-body interaction between the nucleons. With the approximation, the number of terms for the kinetic energy expression (2.1) is A^2 instead of $A(A!)^2$.

In QPD, each nucleon is taken to have a wave packet which is Gaussian in form

$$\chi_a = \left[\frac{\alpha^2}{\pi}\right]^{3/4} \exp\left[\frac{-\alpha^2(\mathbf{r}-\mathbf{r}_a)^2}{2}\right] \exp\left[\frac{i\mathbf{p}_a \cdot \mathbf{r}}{\hbar}\right] . \qquad (2.2)$$

This wave packet is centered at $\mathbf{r}_a$ and has an average momentum $\mathbf{p}_a$. The two-particle antisymmetrized wave function formed from two of these wave packets is

$$\Psi_{ab}(\mathbf{r}_1,\mathbf{r}_2) = \frac{\chi_a(\mathbf{r}_1)\chi_b(\mathbf{r}_2)-\chi_a(\mathbf{r}_2)\chi_b(\mathbf{r}_1)}{[\iint |\chi_a(\mathbf{r}_1)\chi_b(\mathbf{r}_2)-\chi_a(\mathbf{r}_2)\chi_b(\mathbf{r}_1)|^2 \, d\mathbf{r}_1 \, d\mathbf{r}_2]^{1/2}}. \qquad (2.3)$$

The total kinetic energy of a two-body system described by Ψ_{ab} is

$$\langle \hat{K} \rangle_{ab} = \frac{1}{2m}\left[\mathbf{p}_a^2 + \mathbf{p}_b^2 + 3\alpha^2\hbar^2 + \alpha^2\hbar^2 \frac{X_{ab}}{e^{X_{ab}} - 1}\right] \qquad (2.4)$$

where

$$X_{ab} = \frac{1}{2}\left[\alpha^2(\mathbf{r}_a-\mathbf{r}_b)^2 + \frac{(\mathbf{p}_a-\mathbf{p}_b)^2}{(\hbar\alpha)^2}\right].$$

The $3\alpha^2\hbar^2$ term is a result of the uncertainty principle that the wave packet is not a delta function in momentum. The last term of equation (2.4) can be identified as a two-body potential between quasiparticles with phase-space coordinates $(\mathbf{r}_a,\mathbf{p}_a)$ and $(\mathbf{r}_b,\mathbf{p}_b)$. Thus, in QPD the term

$$V_p(X_{ab}) = \frac{(\hbar\alpha)^2}{2m} \frac{X_{ab}}{e^{X_{ab}} - 1} \qquad (2.5)$$

is identified as a candidate form for the Pauli potential between classical quasiparticles which represent fermions. The Pauli potential vanishes when the quasiparticles are well separated in phase space and is repulsive for finite separation in phase space. A system of quasiparticles interacting via the Pauli potential has features[17] which resemble the behavior of a many-particle Fermi gas.

The energy of a system of particles interacting via equation (2.5) (the analogue of the free particle Fermi gas) is

$$E = \frac{(\hbar\alpha)^2}{2m}\left[\sum_l \left(\frac{k_l}{\alpha}\right)^2 + \frac{1}{2}\sum_{l\neq m} \frac{X_{lm}}{e^{X_{lm}} - 1}\right] \qquad (2.6)$$

where

$X_{lm} = \frac{1}{2}(\alpha^2 r_{lm}^2 + k_{lm}^2/\alpha^2)$,

$\mathbf{k}_{lm} = \mathbf{k}_l - \mathbf{k}_m$,

$\mathbf{r}_{lm} = \mathbf{r}_l - \mathbf{r}_m$,

and $\hbar\mathbf{k}_l = \mathbf{p}_l$.

The quasiparticles in the system have labels l and m.

Consider that the quasiparticles of a many-body system are placed in a simple cubic lattice with lattice spacing a. If $a\alpha >> 1$, then the sites are decoupled and the ground state has $\mathbf{k}_l = 0$ for all l. However, this is not the case for smaller separation. One can show[17] that $\mathbf{k}_l = 0$ is not a global minimum of E for $a\alpha < 2.2$, and therefore there exists a ground state of the system at some nonzero $\mathbf{k}_l$.

Having found that the ground state of a system of quasiparticles has non-zero kinetic energy, one can estimate α in equation (2.5) by equating the ground state energy of a system of quasiparticles on a simple cubic lattice with that of an ideal Fermi gas at the same density. However, one finds that equation (2.5) always

underestimates the energy of a Fermi gas for all α. This arises because only two-body terms in the Pauli potential have been used in evaluating the kinetic energy of the many-body system. Therefore, the strength of the Pauli potential has to be rescaled in order to approximate the energetics of the three- and higher-body terms. The Pauli potential is then rewritten as

$$V_p(X_{ab}) = V_s \frac{(\hbar\alpha)^2}{2\,m} \frac{X_{ab}}{e^{X_{ab}-1}} \qquad (2.7)$$

where V_s is the scaling factor. The two parameters of the Pauli potential, V_s and α, are fixed by equating the ground-state energy of a system of quasiparticles on a simple cubic lattice with that of an ideal Fermi gas at the same density over the density range of interest. The best fit of V_s and α is found to be 1.9 and 1/2 fm^{-1} respectively.

To summarize, the Pauli potential is a classical potential that incorporates some of the properties of a system of non-interacting fermions. Its use allows the reduction in the number of terms in an A-body fermion Hamiltonian from $A(A!)^2$ to A^2.

2.3 Nuclear Interaction

In addition to the Pauli potential, the Hamiltonian of a nucleus must include terms arising from the strong and electromagnetic interaction. The nuclear potential energy density is taken to have the following form:[17]

$$V(\mathbf{r}) = \frac{A}{2}\frac{\rho^2}{\rho_o} + \frac{B}{3}\frac{\rho^3}{\rho_o{}^2} + \frac{C}{2}\frac{(\rho_p-\rho_n)^2}{\rho_o} + \frac{g_1}{2}(\nabla\rho)^2 \qquad (2.8)$$

where ρ is the local density at coordinate $\mathbf{r}$, and ρ_o is the density of normal nuclear matter (taken to be 0.17 fm^{-3} here). The third term is used to describe the isospin dependence of the nuclear force and is a function of the local proton density, ρ_p, and the local neutron density, ρ_n. The last term depends on the gradient of the density.

The density of the system is taken to be the direct sum of the density of each quasiparticle ρ_i, such that

$$\rho(\mathbf{r}) = \left(\frac{\alpha^2}{\pi}\right)^{3/2} \sum_i \exp[-\alpha^2(\mathbf{r}-\mathbf{r}_i)^2]. \qquad (2.9)$$

This expression assumes that the cross terms in the $\chi^*\chi$ product of antisymmetrized single-particle wave functions cancel.

Defining $\langle X\rangle_i = \int\rho_i(\mathbf{r})\, X\, d^3r$, equation (2.8) becomes

$$\int V d^3r = \frac{A}{2}\sum_i\left\langle\frac{\rho}{\rho_o}\right\rangle_i + \frac{B}{3}\sum_i\left\langle\frac{\rho^2}{\rho_o{}^2}\right\rangle_i + \frac{C}{2}\int\frac{(\rho_p-\rho_n)^2}{\rho_o}d^3r + \frac{g_1}{2}\int(\nabla\rho)^2 d^3r. \qquad (2.10)$$

All summations but the second one involve of the order of A^2 terms. There are A^3 terms in the summation over $\langle\rho^2/\rho_o{}^2\rangle$. Therefore it is approximated as

$$\sum_i\left\langle\frac{\rho^2}{\rho_o{}^2}\right\rangle_i = \sum_i\left\langle\frac{\rho}{\rho_o}\right\rangle_i^2 + \frac{g_2}{2}\int(\nabla\rho)^2 d^3r \qquad (2.11)$$

which involves A^2 terms. The second term of equation (2.11) vanishes for uniform nuclear matter. However, omission of this term allows unphysical density fluctuations to develop and can lead to ground state instabilities in nuclei heavier than the nucleus with the maximum binding energy per nucleon. Since g_1 and g_2 are parameters of the gradient terms, they can be replaced by $G=g_1+g_2$.

The Coulomb potential between protons is also included in the QPD Hamiltonian. The functional form of the Coulomb potential between two protons with Gaussian charge distributions [i.e. equation (2.2)] contains error functions, which are time consuming to compute. Since this is not a critical part of the calculation, the Gaussian density distribution is replaced with a spherical charge distribution for the purposes of calculating the Coulomb interaction. A spherical charge distribution with radius $r_o=3\sqrt{2\pi/4\alpha}$ has been chosen to give a potential which approximates the exact potential.

By putting equations (2.9) and (2.11) into (2.10) and calculating the integrals, an explicit form for the interaction between the quasiparticles due to the nuclear potential is found. Combining this with the Pauli and Coulomb potentials, the energy of the collection of quasiparticles can be written as

$$H=\frac{1}{2M}\sum_i p_i^2+\frac{1}{2}\sum_{i\neq j}[V_p(X_{ij})+V_c(r_{ij})]+\frac{1}{2}\sum_{ij}\left[\frac{A+CS_iS_j}{\rho_o}+\alpha^2G(3-\alpha^2r_{ij}^2)\right]D(r_{ij})$$

$$+\frac{B}{3\rho_o^2}\sum_i\left[\sum_j D(r_{ij})\right]^2 \qquad (2.12)$$

where

$r_{ij} = |\mathbf{r}_{ij}|$

S_i = 1(-1) for protons (neutrons)

$$V_c(r) = \frac{e^2}{4\pi\varepsilon_o}\begin{cases} 1/r & \text{for } r>r_o \\ \dfrac{3-r^2/r_o^2}{2r_o} & \text{otherwise} \end{cases}$$

$$D(r) = \left[\frac{\alpha}{\sqrt{2\pi}}\right]^3 \exp(-\alpha^2 r^2/2)$$

There are six parameters α, V_s, A, B, C and G in equation (2.12). The value of V_s and α are determined by approximating the properties of zero-temperature Fermi gas as shown in the last section. Four parameters remain to be determined. The method[17] used in determining the parameters is to use three constraints imposed by the infinite nuclear-matter limit so as to reduce the fit to a search over one free parameter. The constraints are as follows:

(i) The binding energy per nucleon of infinite nuclear matter at $\rho=\rho_o=0.17$ fm^{-3} and small $\omega=(\rho_p-\rho_n)/\rho_o$ is taken as $E_B=E_o+a_s\omega^2$ where $E_o=15.68$ MeV, and $a_s=-28.06$ MeV.

(ii) The binding energy has a maximum at $\rho=\rho_o$ and $\omega=0$.

(iii) The energy in the infinite-matter limit can be calculated by using equation (2.8) and the ideal Fermi gas results for the kinetic energy. For small ω, the energy is

$$E(\rho) = \frac{3}{5}\varepsilon_F\left(\frac{\rho}{\rho_o}\right)^{2/3} + \frac{1}{3}\varepsilon_F\left(\frac{\rho}{\rho_o}\right)^{2/3}\omega^2 + \frac{A}{2}\left(\frac{\rho}{\rho_o}\right) + \frac{B}{3}\left(\frac{\rho}{\rho_o}\right)^2 + \frac{C}{2}\left(\frac{\rho}{\rho_o}\right)\omega^2 \tag{2.13}$$

where ε_F is the Fermi energy at $\rho=\rho_o$ and is equal to 38.37 MeV. The binding energy is the difference between the energy in the infinite nuclear-matter limit and the energy when the quasiparticles are infinitely separated.

Therefore, parameters A, B and C can be determined with the above constraints, and a one parameter fit for G can be performed by comparing the calculated binding energies and r.m.s. radii of various nuclei with data.

The ground states of finite nuclei are calculated with the following method. First, the quasiparticles are placed in a body-centered cubic (bcc) lattice and momenta are randomly assigned with a local Fermi gas approximation. The nucleons are propagated under a set of damped equations of motions (based on Hamilton's equations) with the positions and momenta of the quasiparticles as degrees of freedom. The parameter set A=-129.69, B=74.24, C=30.54 MeV, and G=291 MeV-fm^5 produced acceptable ground states.[17] For nuclei with A≥5, it is found that the binding energies and r.m.s. radii are usually within 10% of the experimental values over most of the periodic chart.

2.4 Nucleon-Nucleon Collision Term

As described above, a Hamiltonian for a system of quasiparticles has been developed. Hamilton's equations of motion are used to describe the motion of the quasiparticles. However, such a system is strictly classical and contains none of the randomness associated with quantum mechanics. In order to include at least some aspects of quantum mechanical scattering, a collision term is introduced. The scattering algorithm is chosen to be the following:[17] One test particle is assigned to each quasiparticle according to the Gaussian density distribution of the quasiparticle. If the distance between test particles of two approaching quasiparticles falls below the classical nucleon radius, R_{NN}, an attempt is made to scatter the quasiparticles. The magnitude of R_{NN} is determined by the total in-medium nucleon-nucleon cross section by assuming the simple classical expression, $\sigma_{NN} = \pi R_{NN}^2$. The σ_{NN} is assumed to be isotropic.

At the collision point, the scattering of two particles can be made to conserve both linear and angular momentum. Let $\mathbf{p'}_1$ and $\mathbf{p'}_2$ be the momenta of the test particles after scattering,

$$\mathbf{p'}_1 = \mathbf{p}_1 + S\hat{\mathbf{r}}_{12}\ ,\ \mathbf{p'}_2 = \mathbf{p}_2 - S\hat{\mathbf{r}}_{12} \qquad (2.14)$$

where $\mathbf{p}_i$ is the momentum before scattering, $\hat{\mathbf{r}}_{ij} = \frac{\mathbf{r}_{ij}}{|\mathbf{r}_{ij}|}$ and S is a scalar to be determined from conservation of energy. If energy is conserved, then

$$E'-E = \frac{(\mathbf{p}_1-\mathbf{p}_2)\cdot\hat{\mathbf{r}}_{12}S + S^2}{m} + V(\mathbf{X}_1,\ldots,\mathbf{X}_n,\mathbf{p}_1+S\hat{\mathbf{r}}_{12},\mathbf{p}_2-S\hat{\mathbf{r}}_{12},\mathbf{p}_3,\ldots,\mathbf{p}_n)$$

$$-V(\mathbf{X}_1,\ldots,\mathbf{X}_n,\mathbf{p}_1,\mathbf{p}_2,\mathbf{p}_3,\ldots,\mathbf{p}_n)$$

$$= 0. \qquad (2.15)$$

The secant method is used to determine S. If there is no solution other than S=0, the collision is rejected. Once the new momenta of the scattering pair have been chosen, the collision is accepted if the momenta are not Pauli blocked. (See Ref. 17 for details of the method.) Once the scattering has been accepted, a new test particle is assigned to each quasiparticle.

2.5 Comparison Between BUU and QPD

Let us briefly discuss the numerical techniques used by the BUU model.[20] In the BUU model, each nucleon is represented by N test particles in N samples of the system, i.e. one test particle per nucleon in each sample. The test particles are propagated by Newtonian mechanics with all N samples propagated simultaneously. To evaluate the nuclear potential U or the Pauli blocking term (both of which depend on the local phase space density), the value of the phase space density, f, is calculated by performing an average over all N samples using the number of test particles in the phase space volume of interest. The BUU equation includes scattering of the test particles. For each time step, two test particles of the same sample collide if

(a) the particles pass the point of closest approach;

(b) the distance at closest approach is less than the classical radius of scattering $\sqrt{\sigma_{NN}/\pi}$ where σ_{NN} is the in-medium nucleon-nucleon cross section;

(c) their momenta after the collision are not Pauli blocked.

The directions of the test particles' momenta after the collision are randomly selected from a predetermined distribution (usually assumed to be isotropic in the center-of-mass frame of the two test particles). The magnitudes of the momenta are determined from the conservation of energy and linear momentum. There is no guarantee of conservation of the angular momentum between the pair of test particles. Therefore the angular momentum of the whole nuclear system is not necessarily conserved. However, on average the angular momentum of the system does not change drastically.

A comparison of the BUU model with the QPD model is as follows:

(i) The QPD model is a many-body model in which the correlations between nucleons do not need to be incorporated in a model-dependent fashion. The positions and momenta of the nucleons at any time of the reaction are known. The BUU model is a one-body model. One can only know the probability of having a nucleon at certain point in phase space. One cannot know all the nucleons' positions and momenta simultaneously.

(ii) In BUU-like models, the combined effects of the collision term and numerical integration approximations may lead to ground state nuclei which are unstable on the time scale of a few hundred fm/c. In one model,[13] approximately 1 particle out of 100 leaves the nucleus in the order of 100 fm/c. Therefore, one has to stop the simulation at 100-200 fm/c to avoid possible evaporation of the nuclei. In QPD, the nuclei are in true ground states of the Hamiltonian governing their equations of motion and this allow the reactions to be followed for thousands of fm/c. Because the ground state properties of the nuclei are included in QPD, it is straight-forward to determine quantities such as excitation energy distributions and to follow their time evolution.

Chapter Three

Single Particle Inclusive Spectra

3.1 Introduction

In this chapter, we use the QPD model to simulate a heavy-ion reaction. The properties of the residual nuclei and the single particle inclusive spectra are discussed. Moreover, the results are compared with the experimental results and with the BUU calculation of the same reaction. The layout of this chapter is as follows: In Section 3.2 the simulation of a heavy-ion collision is described. The properties of the residual reaction products and the single particle inclusive spectra for light particles are discussed in Sections 3.3 and 3.4 respectively. Finally, Section 3.5 contains a comparison between QPD and BUU calculations.

3.2 Details of the Simulations

The computer simulations are performed for ^{14}N colliding with ^{154}Sm at 35 A.MeV bombarding energy in the laboratory frame. The corresponding center-of-mass energy per nucleon available to the compound system is 2.6 MeV. The specific projectile, target and bombarding energy of interest are chosen in order to compare the results of the simulation with those of experiments performed at the National Superconducting Cyclotron Laboratory at Michigan State

University.[19] Two data sets are generated. In the first set, a sample of 14,720 events is generated for the impact parameter, b, in the range from 0.5 to 7.5 fm in 1 fm steps. The number of events at each impact parameter is proportional to the area of the ring from b-0.5 to b+0.5 fm. For example, the number of events at b=7.5 fm is 15 times the number at b=0.5 fm. The in-medium nucleon-nucleon (NN) cross section, σ_{NN}, for the simulation is taken as 28 mb. A second data set with 6,400 events of σ_{NN} at 60 mb is also generated over the same impact parameter range. These large event samples are required because of the trigger condition used in the experimental studies: we wish to be able to study the inclusive spectra as well as the circular polarization of the gamma rays emitted as a function of trigger fragment mass, energy and angle. Moreover, we want to compare two sets of data at different in-medium NN cross sections with the experimental results in order to see which σ_{NN} gives the better fit.

For each event, the system of quasiparticles is propagated for 250 fm/c elapsed reaction time. Such an event takes about 4 cpu-minutes to execute on an IBM 3801 mainframe computer. We find that the momenta and excitation energies of most of the reaction products stabilize by about 150 fm/c elapsed time in the reaction where the collision begins about 20 fm/c after the simulation starts. The total execution time for the generation of the two event samples is over 1,000 cpu-hours.

For each event, after the nucleons have been propagated for an elapsed time of 250 fm/c, a cluster search is made over the

nucleons' positions. In the search, quasiparticles whose positions are less than 3.5 fm apart are linked together to form a cluster. The clusters formed are not necessarily in their ground state at this point in the reaction. However, most of the clusters are equilibrated by this time and stable on a time frame of a thousand fm/c, a fact to which we will return in the next section. In other words, these clusters retain their integrity over a longer time scale than that for which it is computationally economical to run the simulation.

3.3 Properties of the Residual Reaction Products

For each event, there is only one heavy residual nucleus which has mass greater than A=150. The other fragments generally have mass less than or equal to the mass of the projectile, A=14. Most of the fragments are unbound nucleons, whose multiplicities are 4.06 and 4.21 for σ_{NN}=28 and 60 mb respectively. The multiplicities of the fragment species decrease with increasing mass of the species. The total multiplicities for A≤14 are 4.95 and 4.97 for σ_{NN}=28 and 60 mb respectively. The difference in total multiplicities calculated from the two in-medium NN cross section is not significant.

In order to study the magnitude of the excitation energy of the residual reaction products, we examine the mass distribution of the residual nuclei. The fractional mass distribution of the residual nuclei of the reaction at σ_{NN}=28 mb is shown in Figure 3.1. The distribution is averaged over impact parameter and normalized over the mass range covered by the figure. It is obvious that most of the

distribution lies at mass greater than the target mass of A=154, which means that some of the mass of the projectile has been transferred to the target. These nucleons are trapped in the residual nucleus which does not decay by the elapsed time when the simulation is stopped.

Suppose we now take a particular nucleus close to the peak of the fractional mass distribution in Fig. 3.1, and evaluate its average excitation energy. We choose the ^{163}Ho nucleus whose ground state energy is -8.34 MeV by the QPD model.[17] The fractional distribution of excitation energy for this nucleus is shown in Fig. 3.2 where the same integration and normalization are chosen as those in Fig. 3.1. There is still a substantial amount of excitation energy remaining in the residual system. The excitation energy of the system found in the reaction with a larger in-medium NN cross section is higher than that of the one with smaller σ_{NN}. Presumably, this arises because there are more nucleon-nucleon collisions at higher σ_{NN} and the system is more thermalized.

In order to study the decay of the residual nuclei in a longer elapsed time frame, we randomly choose 100 and 70 ^{163}Ho nuclei from all residual reaction products at σ_{NN}=28 and 60 mb respectively. Quasiparticles of each residual nucleus are propagated for another 1000 fm/c. It takes about 15 cpu-minutes to execute one event. We find that 12 out of 100 (12%) residual nuclei produced with σ_{NN}=28 mb undergo further decay by emitting one neutron. The rate for those at σ_{NN}=60 mb is 16 out of 70 (23%). We expect that the nuclei produced with σ_{NN}=60 mb will eventually emit more

particles than those at σ_{NN}=28 mb if we allow the simulation to continue to 30,000 fm/c=10^{-19} second, which is the time scale of evaporative decay. In other words, the masses of the residual nuclei at σ_{NN}=60 mb will be less than those at σ_{NN}=28 mb. We have not performed the 30,000 fm/c calculation because it takes over 6 cpu-hours to execute one event. Even if we were to do so, the system may still be excited because (i) the QPD model is a classical model and does not include any decay via tunnelling through the potential barrier; and (ii) the model does not include any decay via the emission of gamma rays for which the time scale is in the order of 10^{-16} second.

Finally, we briefly discuss the systematic errors associated with the QPD code. The errors are associated with non-conservation of linear and angular momentum due to the finite step size of the equation of motion integration routine. The change in energy for a cluster is in the order of 0.1 MeV/A over an elapsed time of 250 fm/c.[17] The change of angular momentum is observed to be less than 1% over an elapsed time of 1000 fm/c. Therefore, the QPD code conserves both energy and angular momentum very well; the main source of error in our predictions is statistical.

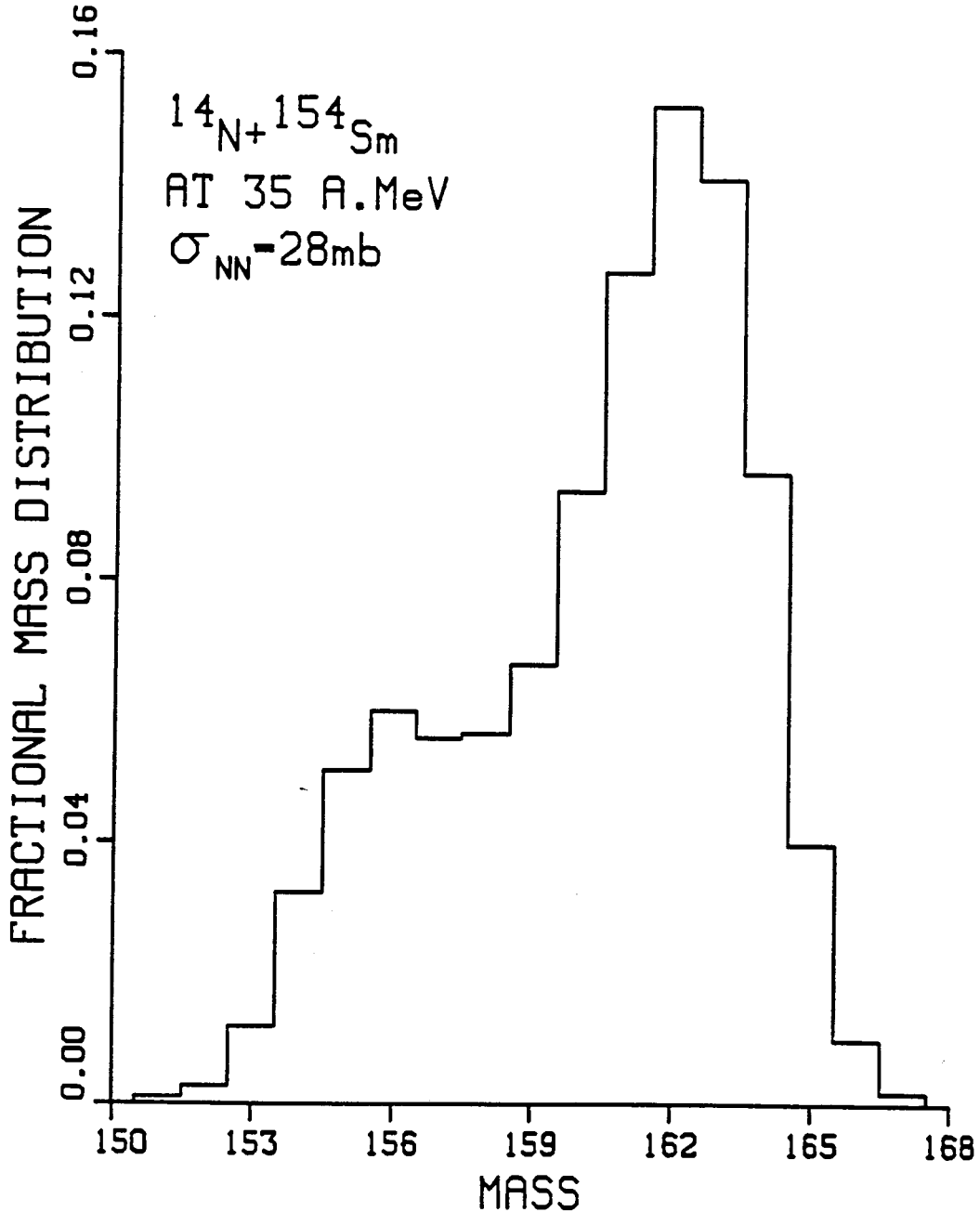

Fig 3.1 Predicted heavy nucleus mass yields for N+Sm at 35 A.MeV, averaged over impact parameter and integrated over fragment energy and angle. The yields are calculated after an elapsed time of 250 fm/c. The distribution is normalized to unity over the fragment mass range shown.

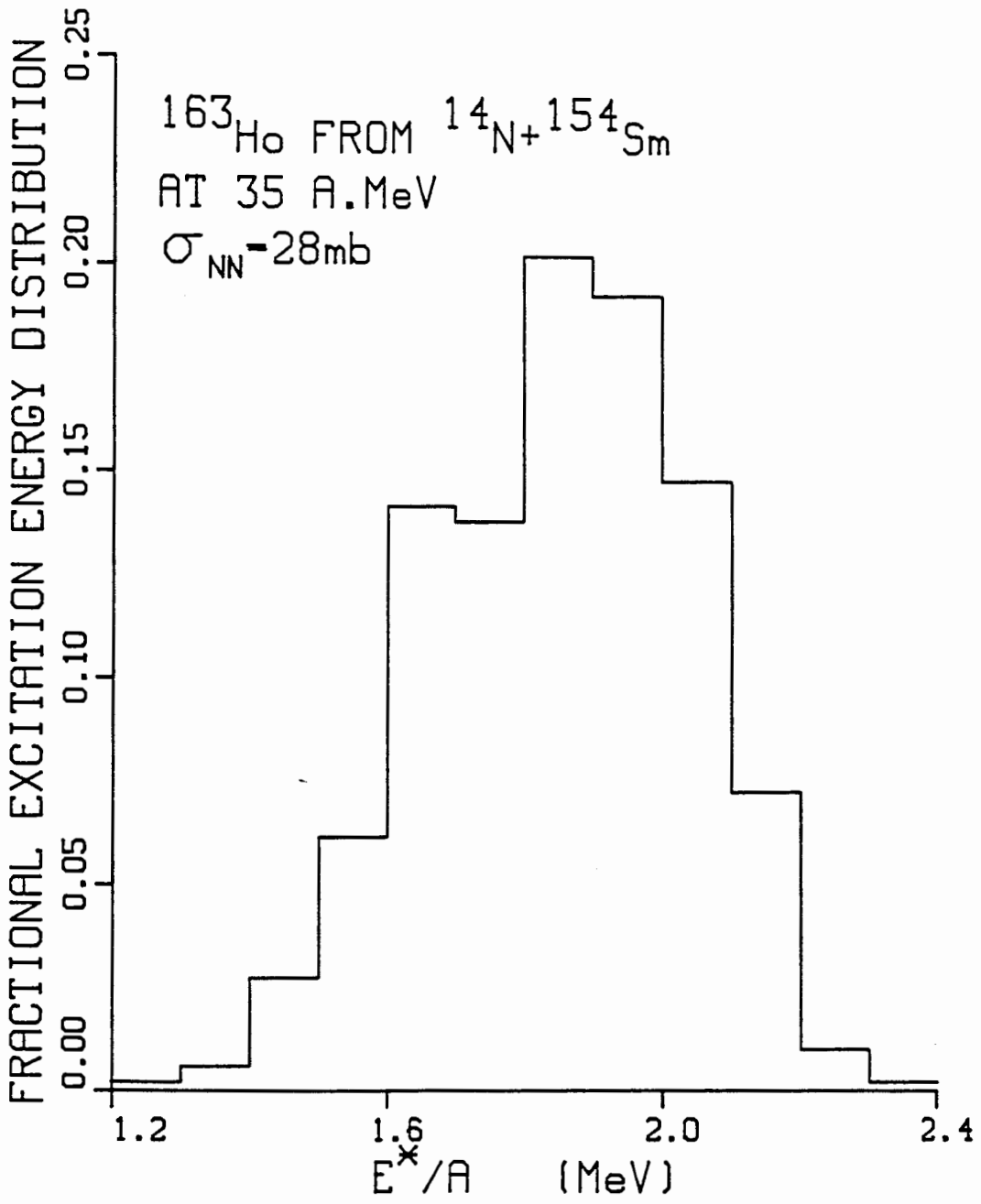

Fig. 3.2 Predicted fractional distribution of excitation energy for the ^{163}Ho nucleus calculated from the simulation of N+Sm at 35 A.MeV, as in Fig. 3.1. The excitation energy is calculated after an elapsed reaction time of 250 fm/c.

3.4 Single Particle Inclusive Spectra for Light Particles

As we have discussed in Chapter One, one of the features of intermediate energy heavy-ion collisions is nonequilibrium particle emission during the equilibration stages of the reaction. These particles can carry kinetic energy per nucleon on the order of that of the projectile. On the other hand, the energy carried by particles emitted from a long-time evaporative decay is usually low. Since we stop the reaction at 250 fm/c which is approximately equal to 10^{-21} second, we assume that products observed in the simulation are predominantly via nonequilibrium emission.

In order to see how well the computer simulation agrees with the experiment, we compare the single particle inclusive measurements of the experiment with the predictions of the simulation. In the experiment,[19] light particles—protons, deuterons, tritons and alpha particles—are detected at polar angles of θ=30° and 60° with respect to the momentum vector of the projectile. Because of our limited statistics, we bin the QPD results into 20° bins centered at 30° and 60° with respect to the beam momentum vector. The differential cross section at (E,θ) is defined as:

$$\frac{d\sigma}{dEd\Omega} = \sum_{b} \frac{A(b)N(b)}{\Delta E \Delta\Omega N_T(b)} \qquad (3.1)$$

where ΔE=10 MeV;

$\Delta\Omega$=-2π[cos(θ+10°)-cos(θ-10°)];

N(b) is the number of particles emitted in $\Delta\Omega$ and within ($E\pm\frac{1}{2}\Delta E$) for reaction at b;

$A(b) = 10\ \pi[(b+0.5)^2 - (b-0.5)^2]$ mb;

$N_T(b)$ is the number of events generated at b.

The proton spectra for emission at 30° and 60° are shown in Figs. 3.3 and 3.4 respectively. The results predicted by the QPD model are indicated by histograms: the dashed curve is for σ_{NN}=28 mb, and the solid curve is for σ_{NN}=60 mb. The experimental data are shown as solid dots. Since the systematic errors in the propagation code are much less than those of the statistical errors, only statistical errors of the predicted spectra are included in Figs 3.3 to 3.8. (All the error bars of the data and some of those of the predicted spectra for Figs. 3.3 to 3.8 are omitted because they are too small). The predicted spectra show the usual behavior: there is a roughly exponential fall-off with emission energy at fixed angle, and a decrease with angle at fixed energy in the laboratory frame. The spectra for the two in-medium NN cross sections at 60° give similar results, while at 30°, the larger in-medium cross section yields a smaller inclusive cross section at proton energies of the order of the beam energy per nucleon.

The calculated and measured inclusive spectra for deuteron clusters at both 30° and 60° are shown in Figs. 3.5 and 3.6 respectively. Although the multiplicities of deuterons are about 20% of the proton multiplicities at any specific σ_{NN}, angle and energy, the deuteron spectra have similar general behavior as the proton spectra. Deuterons from reactions with smaller σ_{NN} correspond to the larger inclusive cross section at forward angles and fragment kinetic energy per nucleon of the order of the beam energy per nucleon. The

agreement between the experiment and predictions is at the two standard deviation level for deuteron fragments with kinetic energy more than 40 MeV at both angles at σ_{NN}=28mb.

The inclusive spectra of triton clusters at both 30° and 60° are shown in Figs. 3.7 and 3.8 respectively. The multiplicities of tritons are only 5% of the proton multiplicities at any specific σ_{NN}, angle and energy. The exponential fall-off with the emission energy of the calculated triton spectra is not as obvious as the proton and deuteron spectra. The shape of both predicted triton spectra at low trigger energy is quite different from that of the data. The agreement is quite good at the high energy part. The agreement between the experiment and the prediction is at the three standard deviation level for triton fragments over 100 MeV at 30° and within two standard deviations at 60° for those tritons with over 60 MeV at both σ_{NN}. The results of alpha-particle clusters are not plotted because the statistics of alpha particle production are poor.

The proton and deuteron spectra at forward angles in Figs. 3.3 and 3.5 show that the reactions at smaller σ_{NN} give larger inclusive cross sections for both triggers at fragment kinetic energies per nucleon larger than the projectile kinetic energy per nucleon. One may have expected that the higher the in-medium NN cross section of the reaction, the higher the single-particle differential cross sections. For example, in simulations of zero impact parameter La+La collisions at 250 A.MeV, the wide angle cross section increases with in-medium cross section. The magnitude of the increase depends on target and

projectile mass: the effect is much less pronounced for Ag+Ag than for La+La.[23]

The results from Fig. 3.3 and 3.5 may appear to be somewhat surprising, taken at face value. What appears to be happening is that the higher the in-medium NN cross section, the greater the number of nucleon-nucleon scatterings. The population of nucleons with kinetic energy in the range of the projectile kinetic energy per nucleon is being reduced by scattering. These nucleons are trapped in excited residual nuclei which have not decayed by the time at which the simulation is stopped. Therefore, the number of fragments emitted at fragment kinetic energies per nucleon in the range of the beam decreases with increasing in-medium NN cross section. On the other hand, the energy-integrated angular distributions do not show a particularly strong dependence on the in-medium NN cross section. This can be seen from Table 3.1, in which the differential cross sections for proton, deuteron, triton and alpha-particle emission are integrated to give a fragment differential multiplicity as function of angle. Results are shown for both σ_{NN}=28 and 60 mb.

		Fragment Species (dN/dΩ)			
Angle	σ_{NN} (mb)	p	d	t	α
30°	28	0.44	0.097	0.020	0.015
30°	60	0.41	0.089	0.014	0.011
60°	28	0.19	0.048	0.017	0.015
60°	60	0.19	0.044	0.018	0.011

Table 3.1: Differential multiplicities of the fragments at different combinations of emission angle and in-medium NN cross section.

The results of the inclusive spectra for protons and deuterons are generally within a factor of 2 of the experimental measurement. As we have discussed in the last section, the excitation energy of the residue is about 2 A.MeV. There should be more decays of the system such as evaporative decay and gamma ray emission in a longer time scale. Since there is no long-time evaporative decay process built into the QPD model,[17] one should be not surprised that the predicted spectra are less than the measured spectra. Since the energy of particles evaporated from heavy residue deexcitation is lower than that of nonequilibrium particles from incomplete fusion reactions, the predicted spectra (especially the low energy part of the spectra) should be higher if evaporation of the excited residual nucleus is considered. Moreover, the masses of the residual nuclei should be smaller after decay. Although the predictions of the reactions at σ_{NN}=28 mb appear to have a better agreement with the experimental data, the experimental data do not necessarily distinguish between either value of σ_{NN}, since the predictions may be changed by long-time-frame decays.

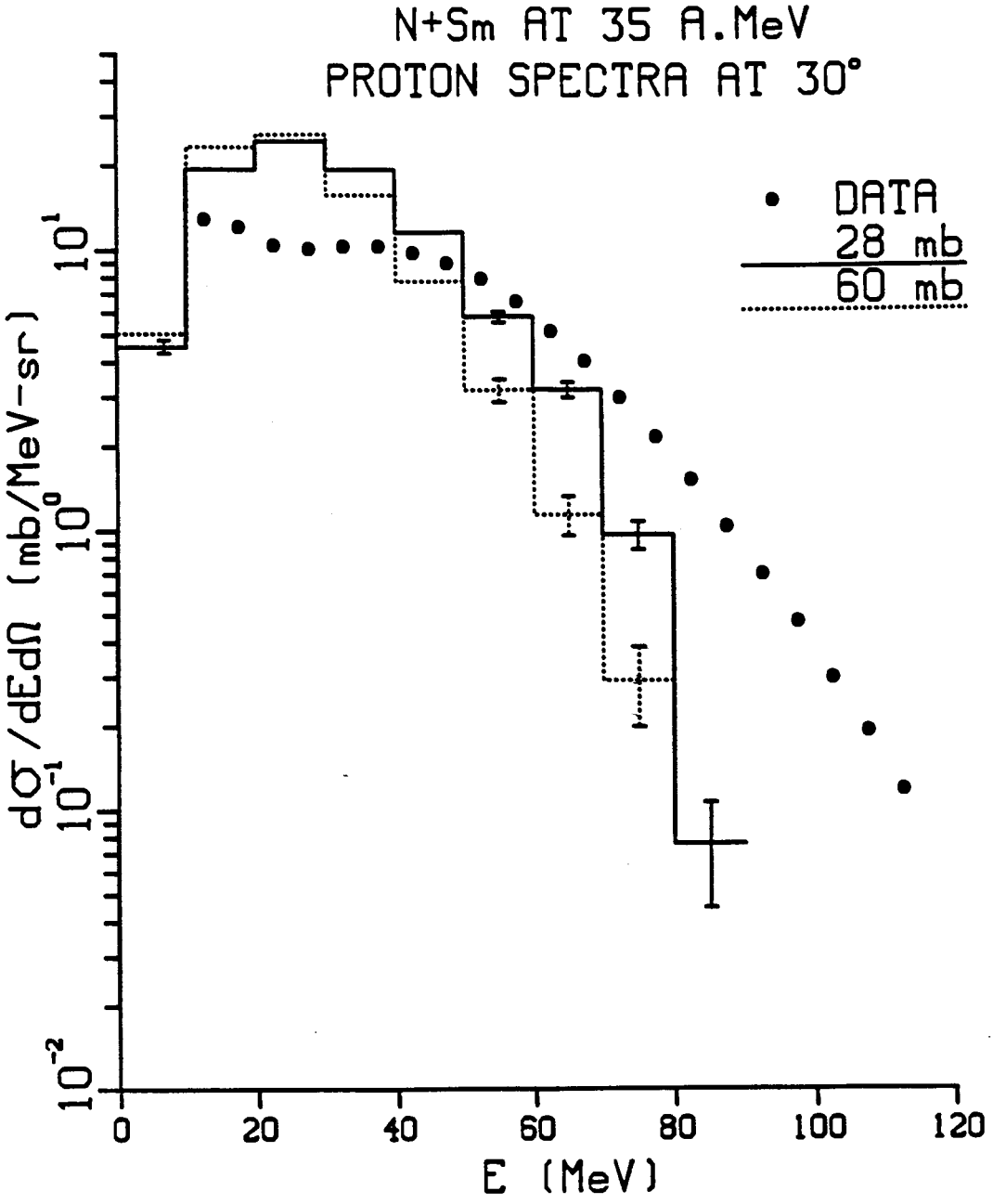

Fig. 3.3 Comparison of experimental data[19] with QPD predictions for proton emission at 30° in N+Sm at 35 A.MeV. The data are shown as the dots, while the predictions are the histograms (solid curve for σ_{NN}=28 mb and dashed curve for 60 mb). The error bars come from statistical errors only.

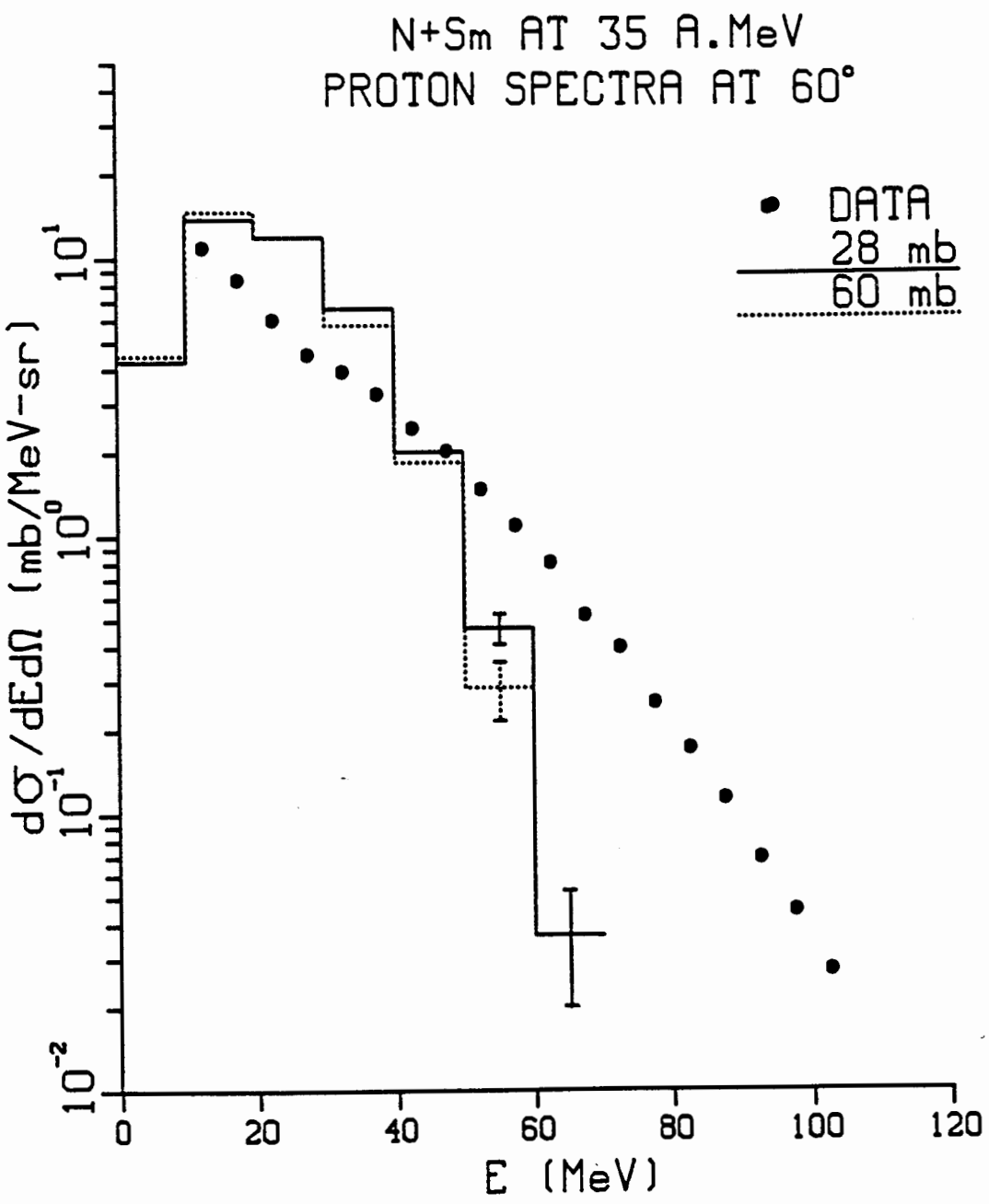

Fig. 3.4 Comparison of experimental data[19] with QPD predictions for proton emission at 60° in N+Sm at 35 A.MeV. The data are shown as the dots, while the predictions are the histograms (solid curve for σ_{NN}=28 mb and dashed curve for 60 mb). The error bars come from statistical errors only.

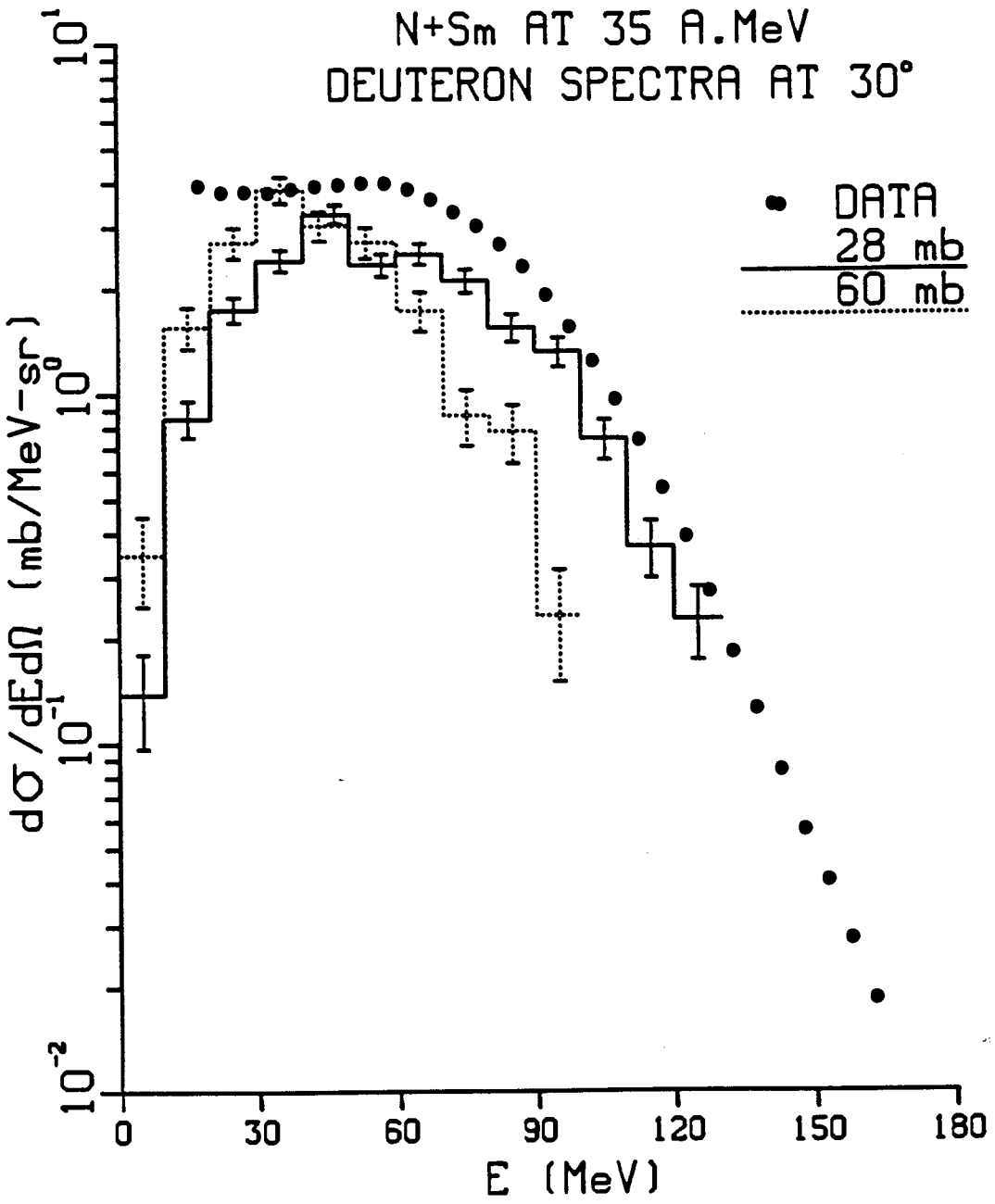

Fig. 3.5 Comparison of experimental data[19] with QPD predictions for deuteron emission at 30° in N+Sm at 35 A.MeV. The data are shown as the dots, while the predictions are the histograms (solid curve for σ_{NN}=28 mb and dashed curve for 60 mb). The error bars come from statistical errors only.

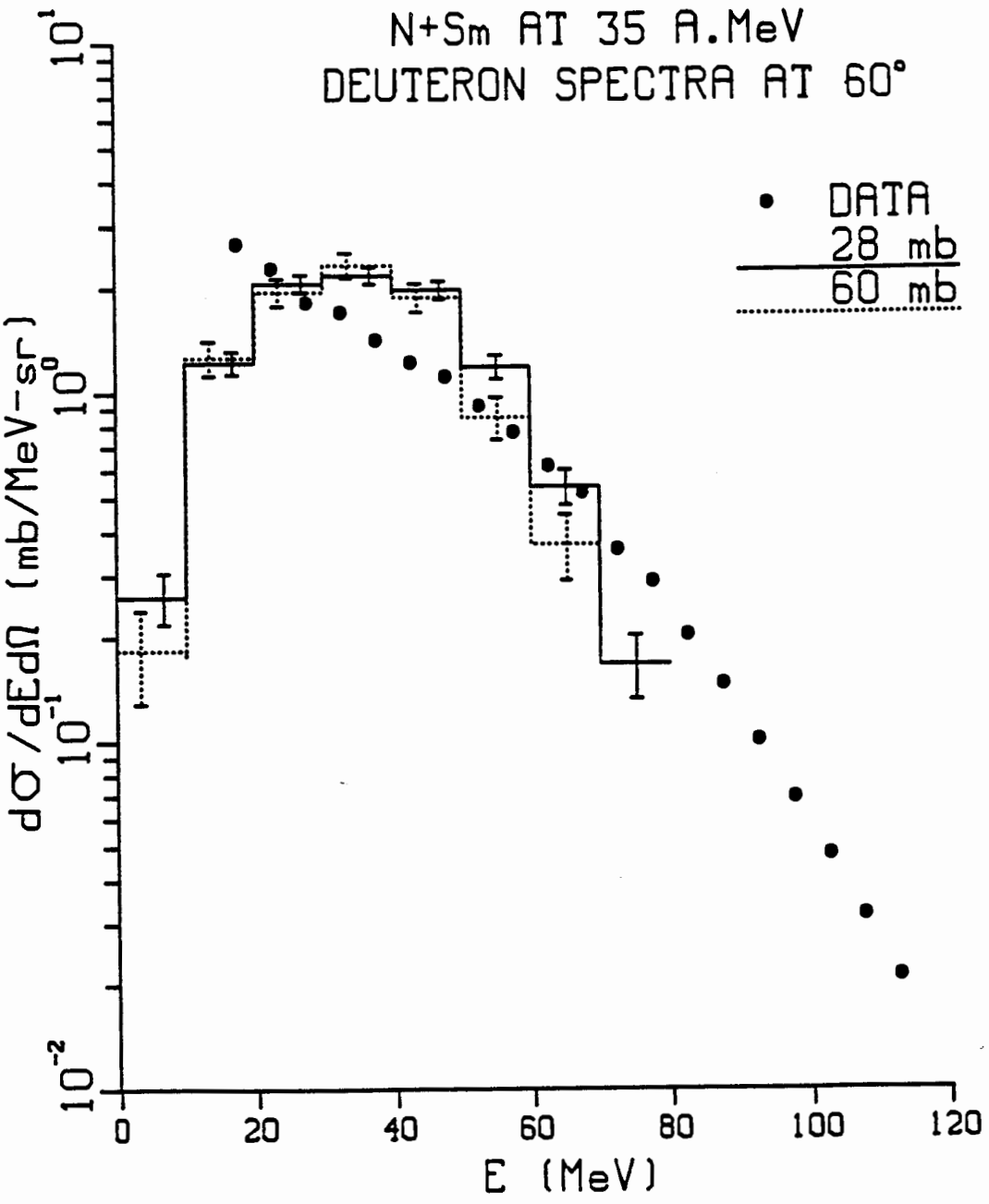

Fig. 3.6 Comparison of experimental data[19] with QPD predictions for deuteron emission at 60° in N+Sm at 35 A.MeV. The data are shown as the dots, while the predictions are the histograms (solid curve for σ_{NN}=28 mb and dashed curve for 60 mb). The error bars come from statistical errors only.

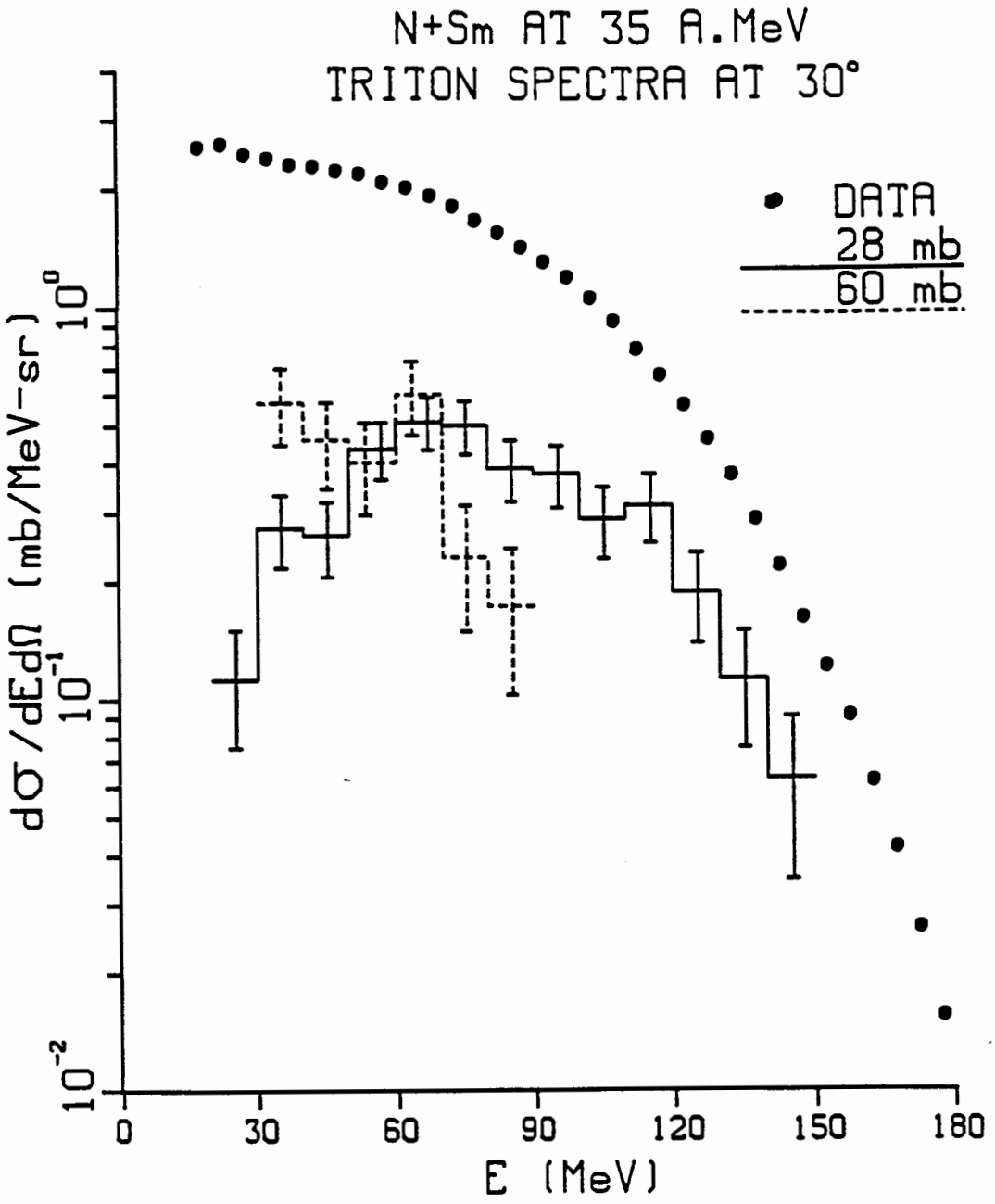

Fig. 3.7 Comparison of experimental data[19] with QPD predictions for triton emission at 30° in N+Sm at 35 A.MeV. The data are shown as the dots, while the predictions are the histograms (solid curve for σ_{NN}=28 mb and dashed curve for 60 mb). The error bars come from statistical errors only.

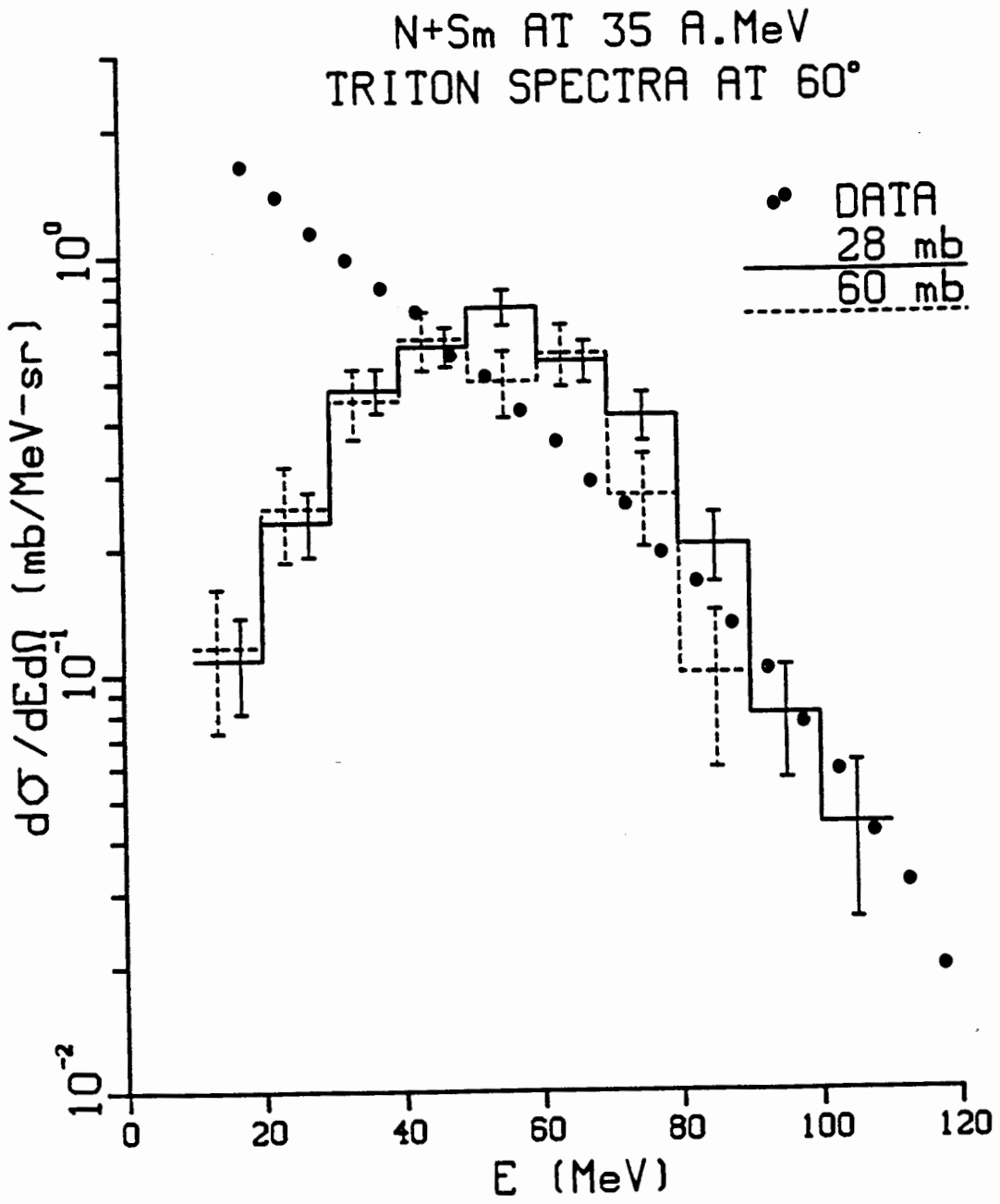

Fig. 3.8 Comparison of experimental data[19] with QPD predictions for triton emission at 60° in N+Sm at 35 A.MeV. The data are shown as the dots, while the predictions are the histograms (solid curve for σ_{NN}=28 mb and dashed curve for 60 mb). The error bars come from statistical errors only.

3.5 Comparison Between QPD and BUU Calculations

It is worthwhile to compare the results calculated from the QPD model with those found in a BUU calculation.[22] When we compare the single particle inclusive spectra from the QPD simulation with those from the BUU calculations, certain rearrangements of the QPD results should be made. BUU calculations do not give the free nucleon spectrum directly: an assumption has to be made in the BUU model to extract it from the one-body distribution of nucleons in phase space. A commonly adopted procedure is to evaluate the local coordinate space density in a region to determine the strength of the nuclear mean field, and from this extract the fraction of nucleons in that region which are unbound.

In Ref. 22, a calculation of the same heavy ion reaction is performed in the BUU model for an elapsed reaction time of 200 fm/c. In the analysis of the simulation, individual nucleons are assumed to be contained in a fragment if the sum of their kinetic energy and the local $U(\rho)$ which they experience is less than 6 MeV where

$$U(\rho) = -356\left(\frac{\rho}{\rho_o}\right) + 303\left(\frac{\rho}{\rho_o}\right)^{7/6} \text{ MeV}; \qquad (3.2)$$

and ρ is the local density. Otherwise nucleons are assumed to be unbound. Under this condition, the fast unbound nucleons and the bound residues are clearly separated. BUU predicts that the target-like residual nuclei have mass of approximately 150 nucleons and will continue to decrease in mass with increasing elapsed time of the calculation due to compound evaporation processes. The average

mass of the residual nuclei calculated here by the QPD model is approximately 10 mass units heavier than that found by the BUU model. However, a 'cold' nucleus in its ground state can evaporate nucleons on the time scale of a few hundred fm/c in a BUU calculation.[13] Hence, it is not certain whether the evaporation predicted by the BUU model is due to the numerical instability of the model or to a good approximation of the evaporation process.

In order to more directly compare our predictions with the BUU calculation, the proton and neutron cross sections from the QPD simulation are summed up. The spectra for mass A=1 at 30° and 60° are shown in Figs. 3.9 and 3.10 respectively. The BUU results for the nucleon cross section are calculated with in-medium NN cross section at 20 and 41 mb. (Some error bars for both figures are omitted because they are too small.) The spectra from the results of the two models are similar in shape. The spectra from the BUU calculation are at a factor of two-three higher in magnitude than those from the QPD simulation. The reasons for the difference may be: (i) there is still substantial excitation energy in the residual nuclei at the time when the QPD simulation is stopped; and (ii) the QPD spectra do not include the light particles with mass A>1 whereas the BUU spectra include all nucleons which are not bound within the residual nuclei. Given the different definition of the observables in the two models, the agreement is in the range expected. Lastly, the BUU results for the integrated nucleon cross section do not show strong sensitivity to σ_{NN} in the 20-41 mb range, which is similar to what is found in the QPD model.

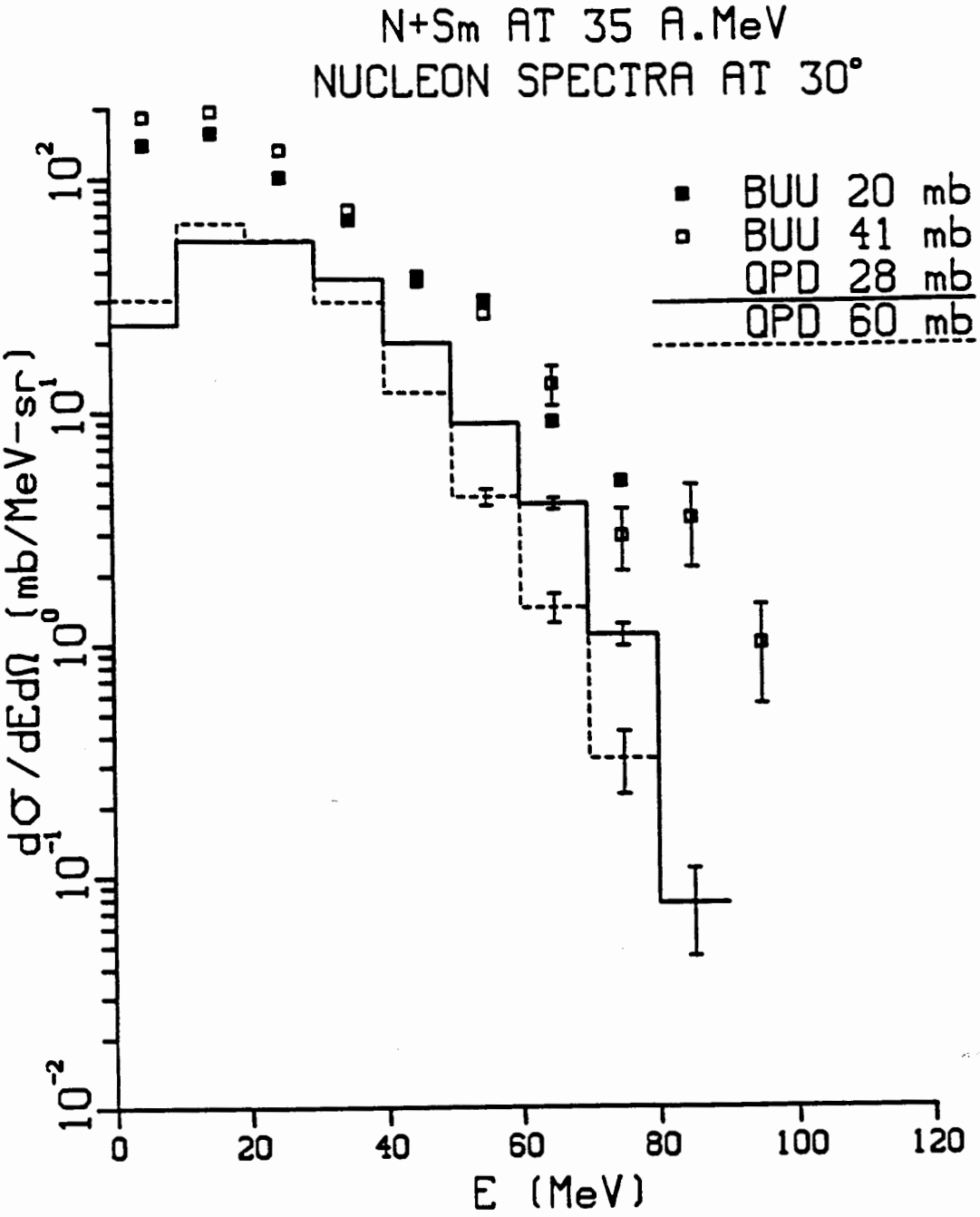

Fig. 3.9 Comparison of BUU[22] calculations with QPD predictions for nucleon emission at 30° in N+Sm at 35 A.MeV. The BUU results are shown as squares (solid square for σ_{NN}=20 mb and hollow square for 41 mb), while the QPD predictions are the histograms (solid curve for σ_{NN}=28 mb and dashed curve for 60 mb). The error bars of the QPD predictions come from statistical errors only.

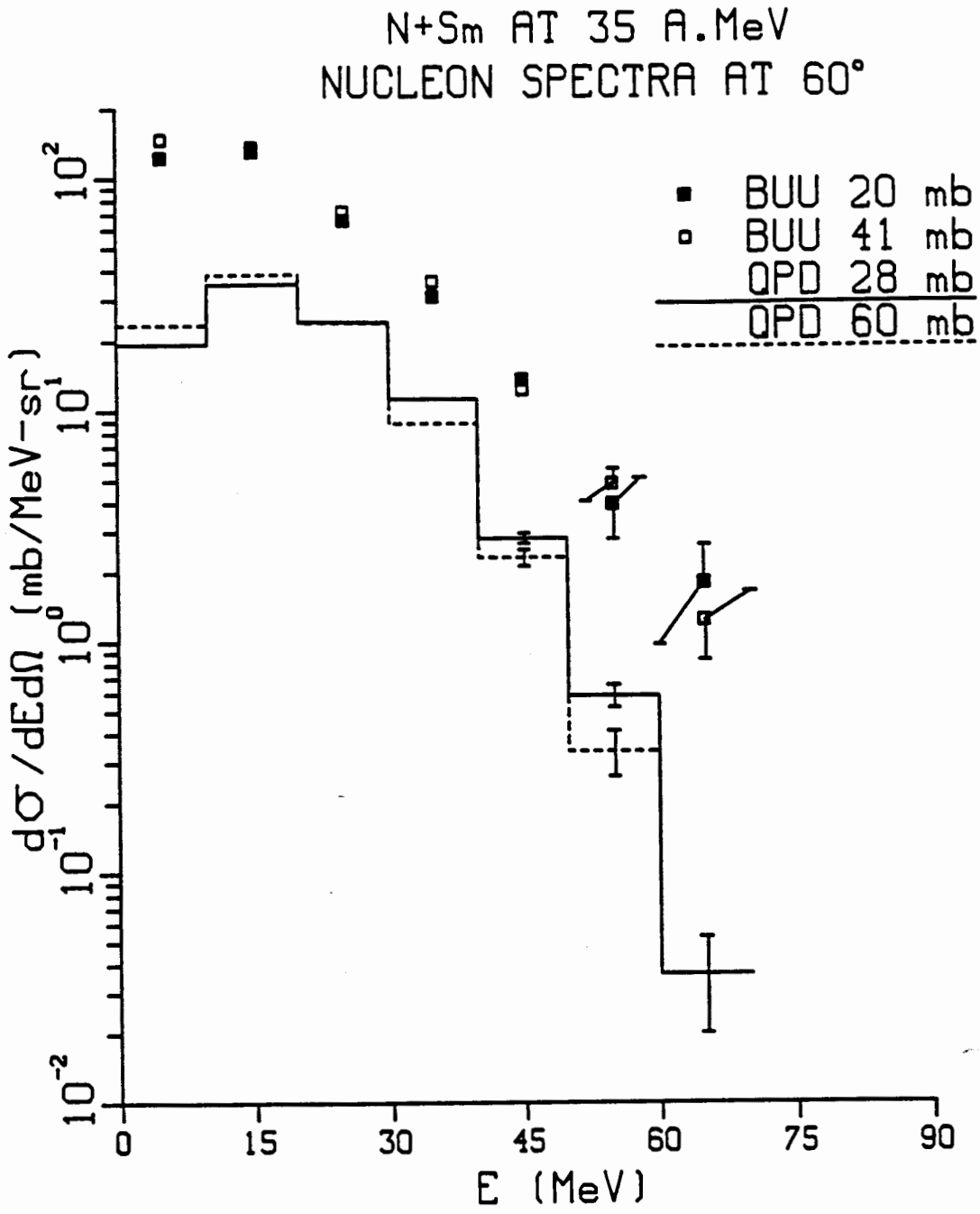

Fig. 3.10 Comparison of BUU[22] calculations with QPD predictions for nucleon emission at 60° in N+Sm at 35 A.MeV. The BUU results are shown as squares (solid square for σ_{NN}=20 mb and hollow square for 41 mb), while the QPD predictions are the histograms (solid curve for σ_{NN}=28 mb and dashed curve for 60 mb). The error bars of the QPD predictions come from statistical errors only.

Chapter Four

Gamma Ray Circular Polarization

4.1 Introduction

In the last chapter, we showed that the single particle inclusive spectra predicted by the QPD model give reasonable agreement with experiment. However, such comparisons reveal little of the relationship between the reaction dynamics and the nonequilibrium particles emitted. Nor do they show any azimuthal anisotropies of the light particles emitted. For example, one question of interest is the correlation between the trigger plane and the reaction plane. Such effects can only be revealed by more complex coincidence measurements.

The first experimental evidence that nonequilibrium light particle emission from fusion-like reactions exhibit large azimuthal asymmetries was obtained from ^{14}N induced reactions on ^{197}Au at E/A=30 MeV.[18] The data show that nonequilibrium light particles are emitted preferentially in the plane perpendicular to the entrance channel orbital angular momentum, indicating there is a collective motion in the plane and transverse to the beam axis. Microscopic calculations with the BUU equation interpret this effect in terms of a deflection to negative emission angles by the attractive nuclear mean field.[14] However, the collective motion in the nuclear mean field is damped by nucleon-nucleon collisions. The relative importance of

positive and negative emission angles is sensitive to the interplay between the nuclear mean field and nucleon-nucleon collisions.

Tsang and co-workers address these issues experimentally by determining the circular polarization of gamma rays emitted by the residual nucleus in coincidence with the nonequilibrium light particle emission for the reaction ^{14}N on ^{154}Sm at E/A = 35 MeV.[19] They observe that the gamma rays are positively circularly polarized, which corresponds to negative deflection angles as discussed in Chapter One. In this chapter, we use the QPD model to predict the gamma rays' circular polarization, and to study the correlation between the trigger plane and the reaction plane. The results are compared with those of the experiments and those calculated with the BUU model in Sections 4.3 and 4.4 respectively. Finally, the microscopic dynamics of the collision process is studied in Section 4.5.

4.2 Methodology

The measurements of the circular polarization of gamma rays emitted by the residual nuclei in coincidence with the emission of light particle triggers are performed at the National Superconducting Cyclotron Laboratory of Michigan State University.[19] The method of detecting the light particles is described in the last chapter. The polarimeter to measure the circular polarization of gamma rays emitted defines a quantization axis, perpendicular to the trigger

plane. The details of the experimental set up are thoroughly discussed in Refs. 19 and 24.

The QPD model can give information about the positions, momenta, excitation energies and angular momenta of clusters at any time during the reaction. It does not include any mechanism for dealing with gamma ray emission. In order to calculate the circular polarization of the gamma rays, we adopt a model advanced in Ref. 19 in which the spin deexcitation of the heavy residual nucleus is assumed to proceed via stretched E2 transitions. Such transitions have a gamma ray multiplicity of $M=|\mathbf{J}|/2$ for a residual nucleus with angular momentum $\mathbf{J}$. In the calculation, we only consider the orbital angular momentum of the nucleus and ignore the intrinsic spin of the nucleons.

Before we go on any further, let us discuss the labelling convention for the vectors involved in the circular polarization calculation, as shown in Figure 4.1. The momenta of the beam, $\mathbf{k}_i$, and the trigger fragment, $\mathbf{k}_f$, are used to define a trigger plane. The quantization axis $\hat{\mathbf{n}}_{if}$ is defined by $\hat{\mathbf{n}}_{if}=\frac{\mathbf{k}_i\times\mathbf{k}_f}{|\mathbf{k}_i\times\mathbf{k}_f|}$ at which the polarimeter is located. The initial reaction plane, defined by the beam direction and the impact parameter vector $\mathbf{b}$ lies at an angle ϕ with respect to the trigger plane.

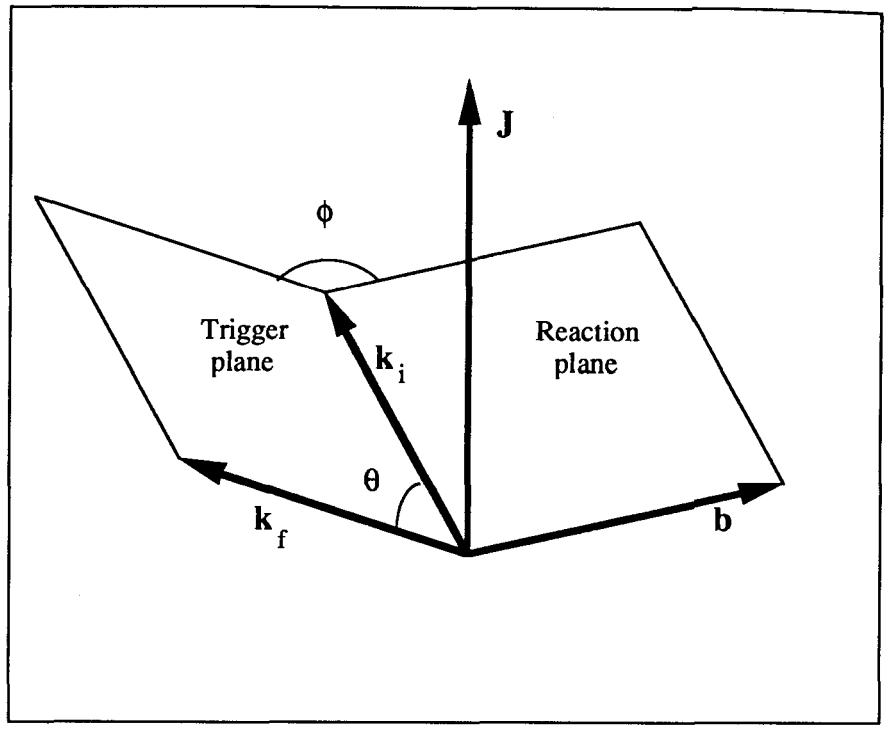

Fig. 4.1 Sign convention for vectors and planes involved in the circular polarization determination. The vector **J** is the orbital angular momentum of the residual nucleus. The momentum vector of the beam $\mathbf{k}_i$ and that of the trigger $\mathbf{k}_f$ form the trigger plane. The impact parameter vector **b** and $\mathbf{k}_i$ form the reaction plane.

For each simulation event, there is only one large residual nucleus present, and its angular momentum vector is used to calculate the characteristics of the emitted gamma rays. In the stretched E2 cascade, gamma rays with momentum **k** are emitted from the residual nucleus with an angular distribution,

$$Y(\beta) = 1 - \cos^4(\beta) \qquad (4.1)$$

where

$$\cos(\beta) = \frac{\mathbf{k}\cdot\mathbf{J}}{|\mathbf{k}\cdot\mathbf{J}|}. \qquad (4.2)$$

The circular polarization of gamma ray is then:

$$P(\beta) = \frac{2\cos(\beta)}{1+\cos^2(\beta)}. \qquad (4.3)$$

The polarization measured with a trigger fragment angle and energy (θ,E) is given by

$$P(\theta,E) = \frac{< M\int d\Omega P(\beta)Y(\beta) >}{<M\int d\Omega Y(\beta) >} \qquad (4.5)$$

where the average is taken over those events which satisfy the trigger conditions. The simulation event sample is the same as described in the last chapter. The integrals at both the numerator and the denominator of equation (4.5) are analytically integrated over the geometry of the polarimeter[24] which covers a polar angle from 20° to 45° with respect to the quantization axis, $\hat{\mathbf{n}}$, and the full range of azimuthal angles, 2π. Equation (4.5) becomes

$$P(\theta,E) = \frac{<M\pi(0.766\cos\psi - 0.530\cos^3\psi - 0.354\cos\psi\sin^2\psi) >}{<M\pi(0.465 - 0.222\cos^4\psi - 0.0197\sin^4\psi - 0.210\sin^2\psi\cos^2\psi) >} \qquad (4.6)$$

where ψ is the angle between the angular momentum vector of the residual nucleus, $\mathbf{J}$, and the quantization axis, $\hat{\mathbf{n}}$. If $\mathbf{J}$ is parallel to $\hat{\mathbf{n}}$, equation (4.6) gives the calculated maximum circular polarization, P_{max}, of 0.97.

If we write Eq. 4.6 as

$$P(\theta,E) = \frac{< T >}{< B >},$$

then the statistical errors for the circular polarization are

$$\Delta P(\theta,E) = <P>\left[\frac{\sqrt{<(T - < T >)^2 >}}{< T >} + \frac{\sqrt{<(B - < B >)^2 >}}{< B >} \right]$$

4.3 Results of the Calculation

We begin with an overview of the behavior of the calculated circular polarization. In Figure 4.2, we show the dependence of the predicted polarization on fragment trigger mass and kinetic energy. (Since the systematical errors which are arrived from the uncertainties of the conservation of angular momentum are much less than the statistical errors, only statistical errors are included in all predicted circular polarization plots from Figs. 4.2 to 4.8). The trigger angle is fixed at 30° and the in-medium NN cross section is chosen as 28 mb. Positive circular polarizations are observed for all trigger masses and kinetic energies. There are two trends: the circular polarization increases with the trigger mass and kinetic energy. These trends are qualitatively similar to what is observed experimentally.

The dependence of trigger angle and kinetic energy for protons and deuterons (both at σ_{NN}=28 mb) are shown at Figures 4.3 and 4.4

respectively. For proton triggers, there is little difference in the circular polarization calculated at 30° and at 60°. For deuteron triggers, the angular dependence is more pronounced: the circular polarization increases with trigger angle. The trigger energy dependence shows a similar trend for both trigger fragment masses at both angles: circular polarization increases with trigger energy. These observations qualitatively agree with what is measured experimentally. We do not calculate the circular polarization at wider angles for either trigger fragments because we do not have enough statistics to draw any conclusion.

Figures 4.5 and 4.6 show the calculated circular polarization at two in-medium NN cross sections and the experimentally measured one for proton triggers at 30° and at 60° respectively. It is obvious that the circular polarization predicted by the computer simulation decreases with increasing in-medium NN cross section. This is because more nucleon-nucleon collisions in the reaction with larger in-medium NN cross section tend to reduce the angular momentum alignment of the residual nucleus. The effect of decreasing circular polarization with increasing σ_{NN} is also seen in deuteron and triton triggers. Figures 4.7 and 4.8 show the results of the deuteron triggers.

As shown in Figs. 4.5 to 4.8, the calculated circular polarizations are much higher than the measured ones. In Fig. 4.5, the calculated and the measured circular polarizations for proton triggers at energy below 40 MeV at 30° in σ_{NN}=60mb disagree by several standard deviations. The agreement for deuteron triggers at low energies at

30° and σ_{NN}=60mb is within their uncertainty ranges but the errors are large. There are two reasons to explain the discrepancy between our predictions and the data:

(i) When the simulations are stopped at an elapsed time of 250 fm/c, the systems are still highly excited. Evaporative decays tend to dealign the final residue angular momentum compared to the initial orbital angular momentum. Thus, the circular polarization is diminished. When a statistical code[24] was used to provide an estimate of such effect, it was found that the predicted circular polarization could decrease by as much as 30%.

(ii) When we do the calculation, we assume all the gamma ray emission is via stretched E2 transitions. If other nonstretched transitions are considered, the circular polarization can be reduced by 20%.[25]

However, the predicted circular polarizations are still be higher than the data even if the above factors are considered.

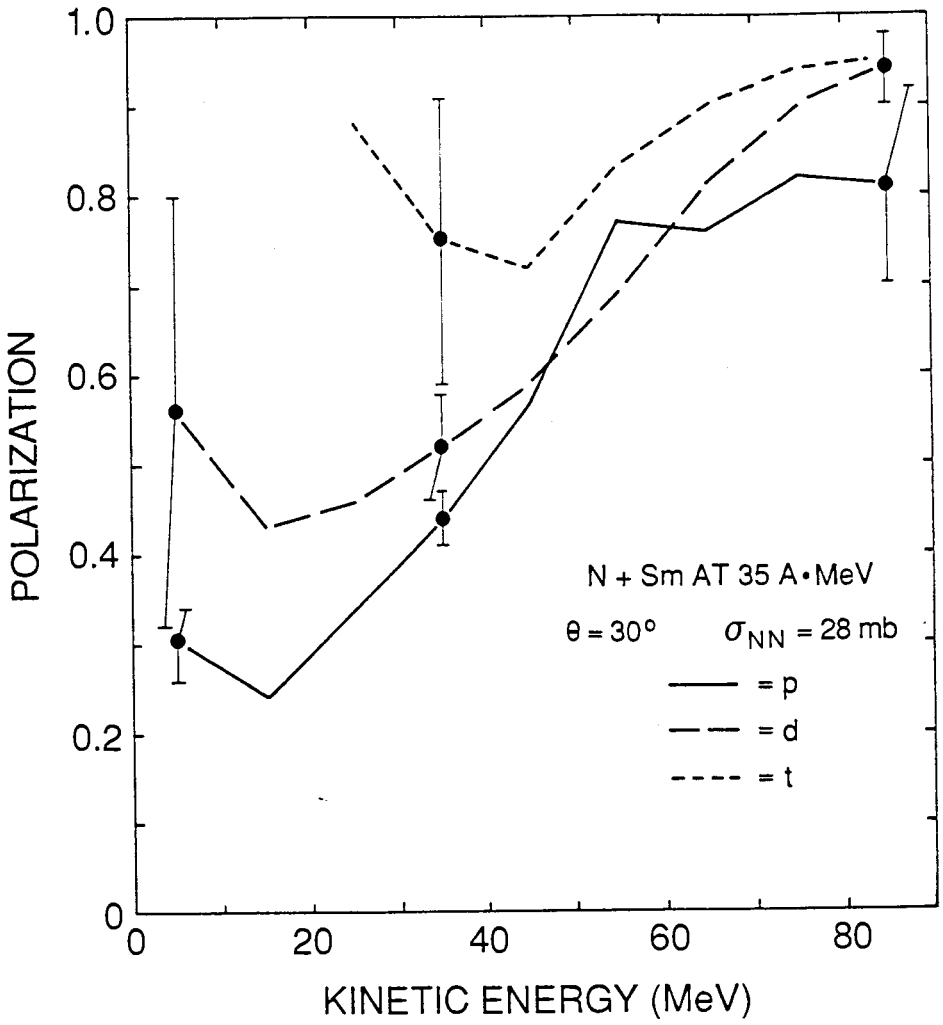

Fig. 4.2 Predicted trigger mass and energy dependence of circular polarization observed at 30°. An in-medium NN cross section of 28 mb is used for the calculation. The results are for the reaction N+Sm at 35 A.MeV and are averaged over impact parameter. Selected statistical error bars are included.

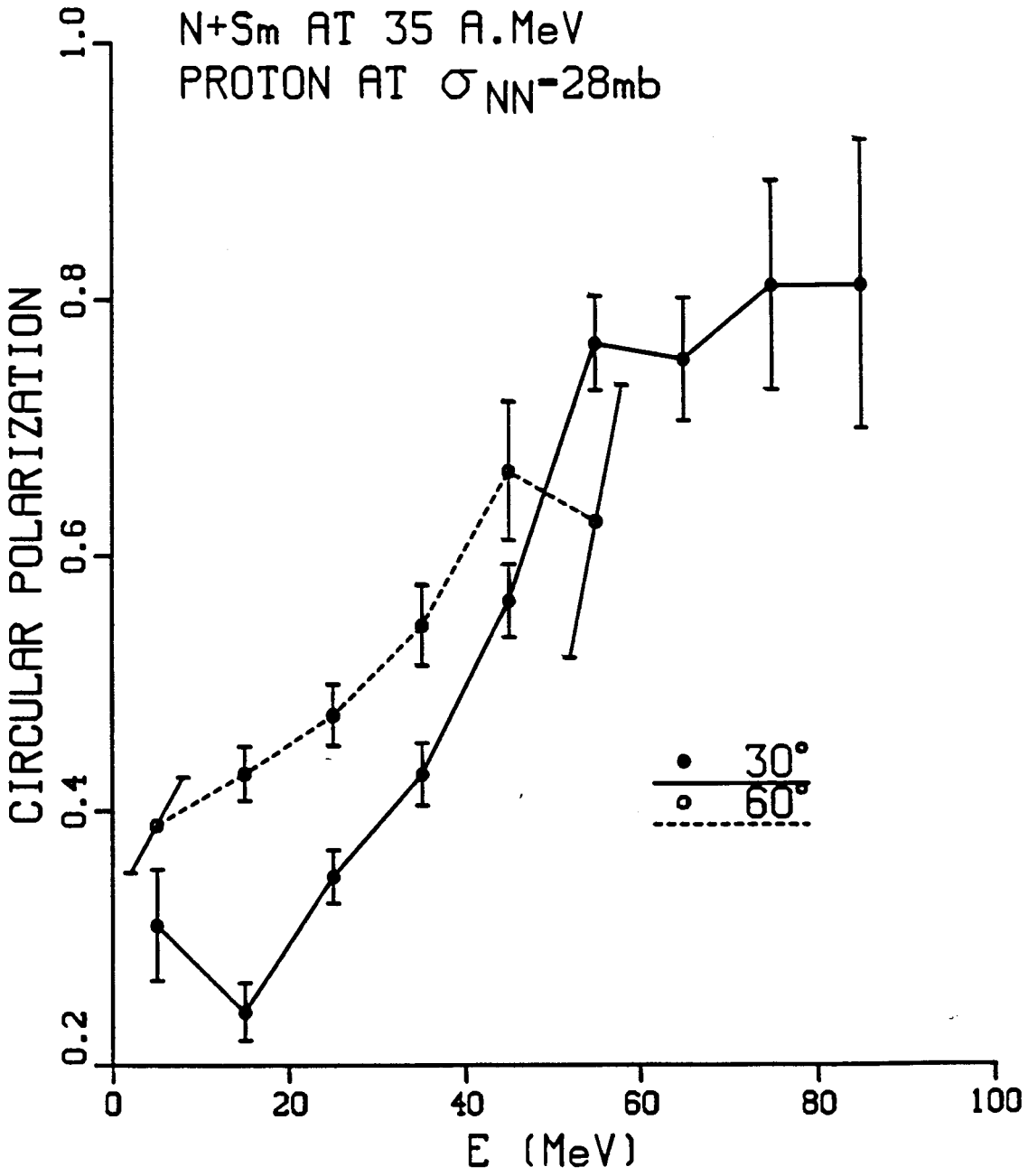

Fig. 4.3 Predicted proton trigger emission energy dependence of circular polarization shown at both 30° and 60°. Other conditions are as in Fig. 4.2. Statistical error bars are included.

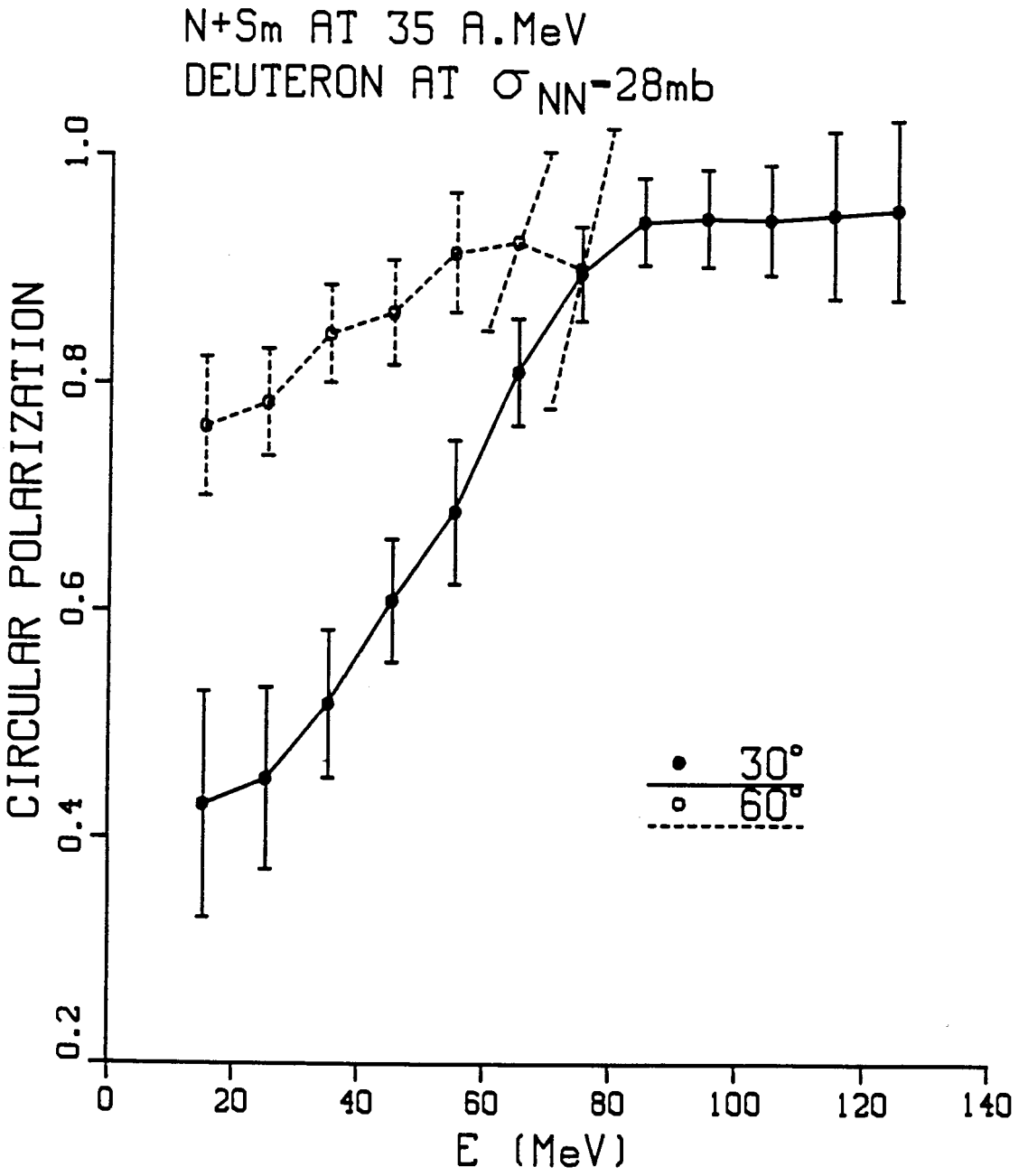

Fig. 4.4 Predicted deuteron trigger emission energy dependence of circular polarization shown at both 30° and 60°. Other conditions are as in Fig. 4.2. Statistical error bars are included.

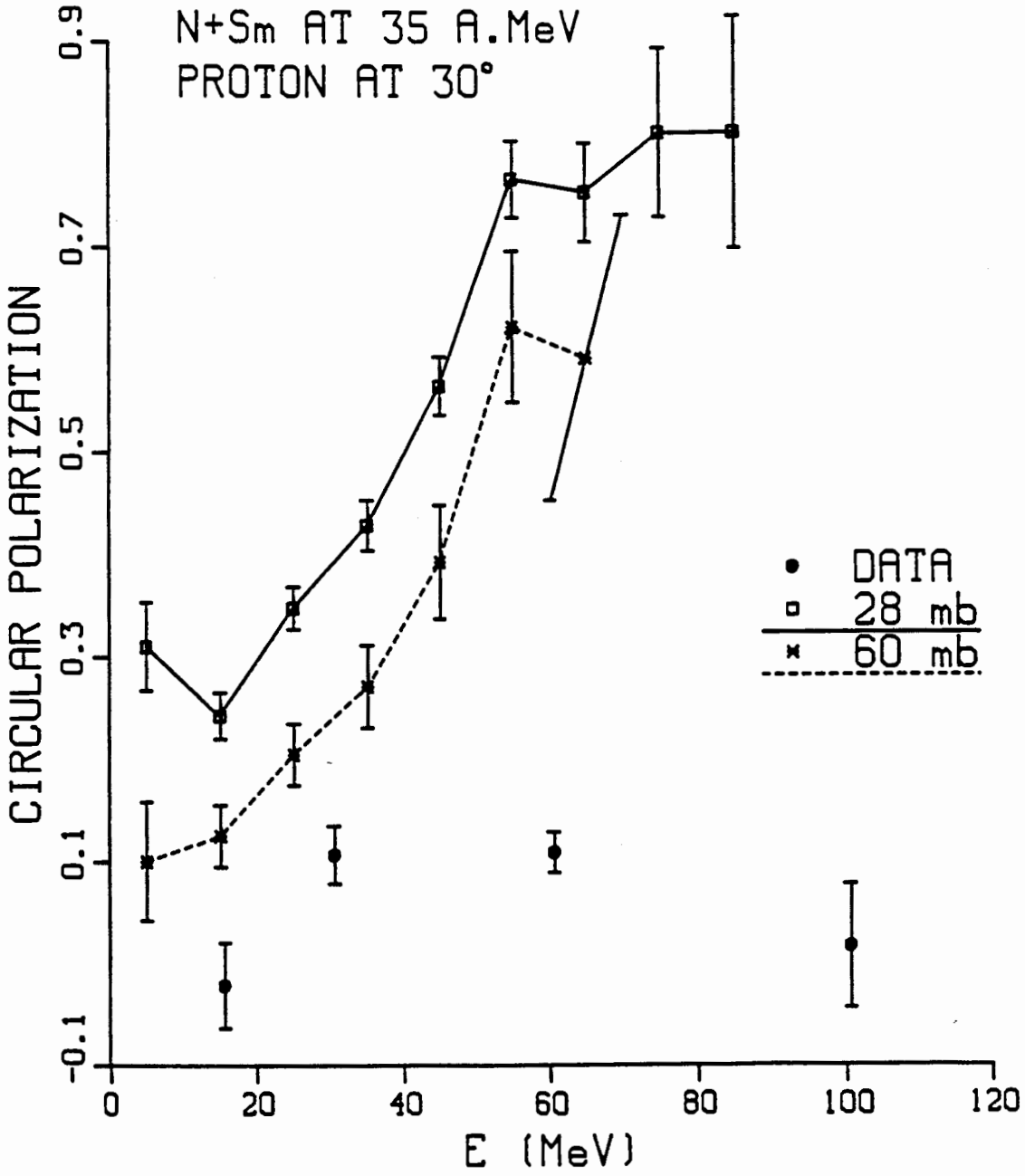

Fig. 4.5 Comparison of simulation and experiment for proton triggered events at 30°. Two values of σ_{NN} were used in the simulation: 28 and 60 mb. Data are from Ref. 19. Statistical error bars of simulation are included.

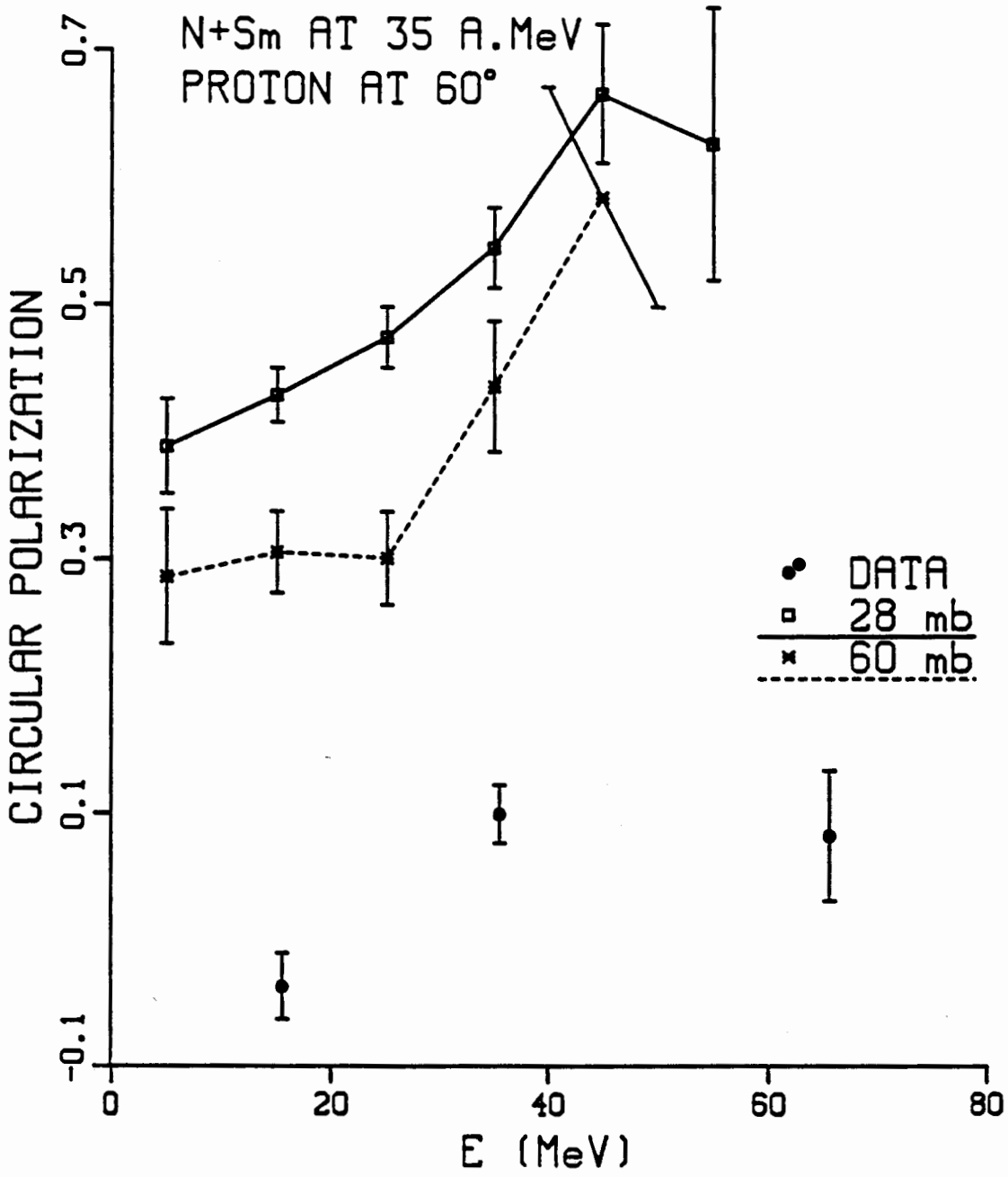

Fig. 4.6 Comparison of simulation and experiment for proton triggered events at 60°. Two values of σ_{NN} were used in the simulation: 28 and 60 mb. Data are from Ref. 19. Statistical error bars of simulations are included.

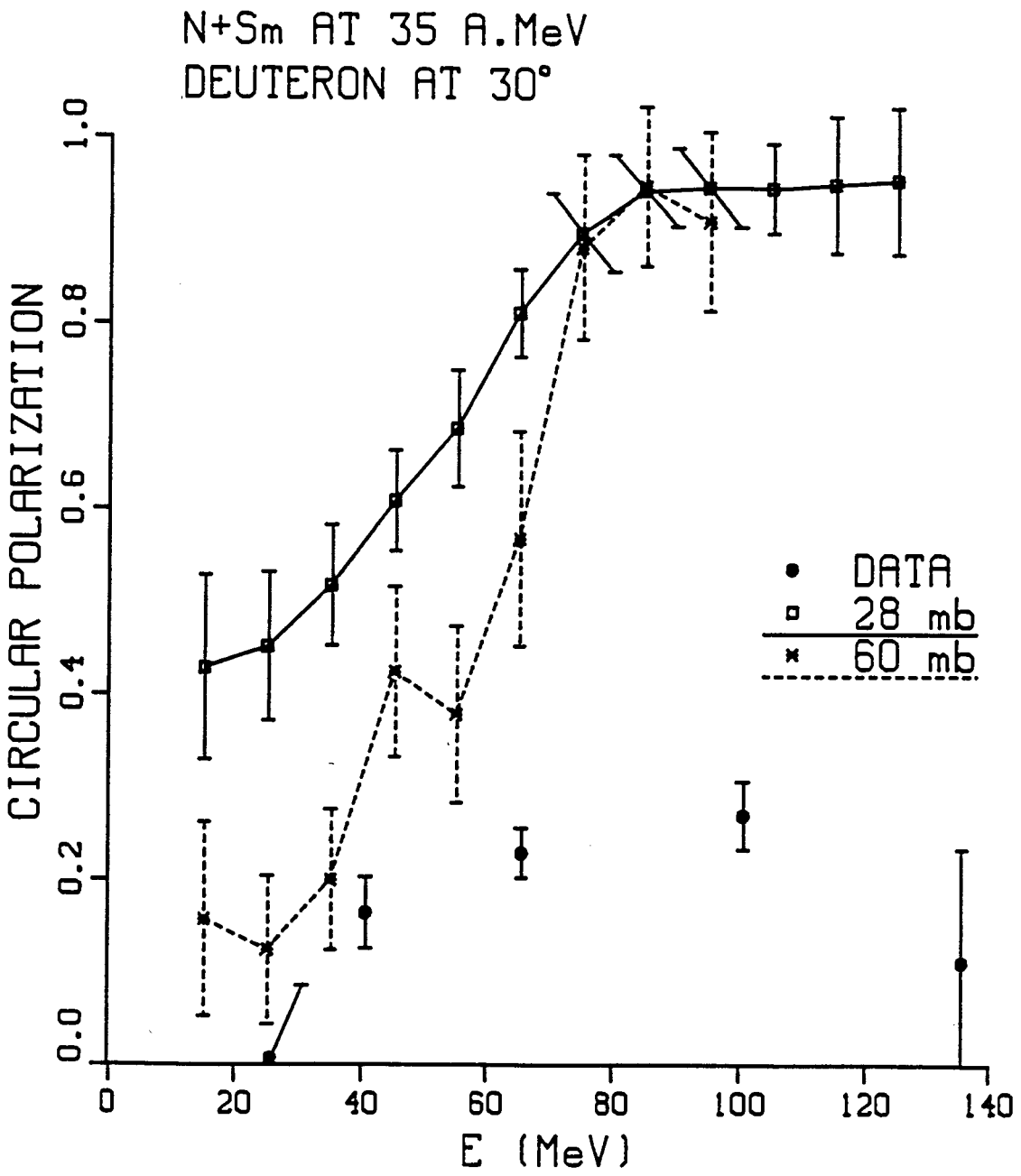

Fig. 4.7 Comparison of simulation and experiment for deuteron triggered events at 30°. Two values of σ_{NN} were used in the simulation: 28 and 60 mb. Data are from Ref. 19. Statistical error bars of simulation are included.

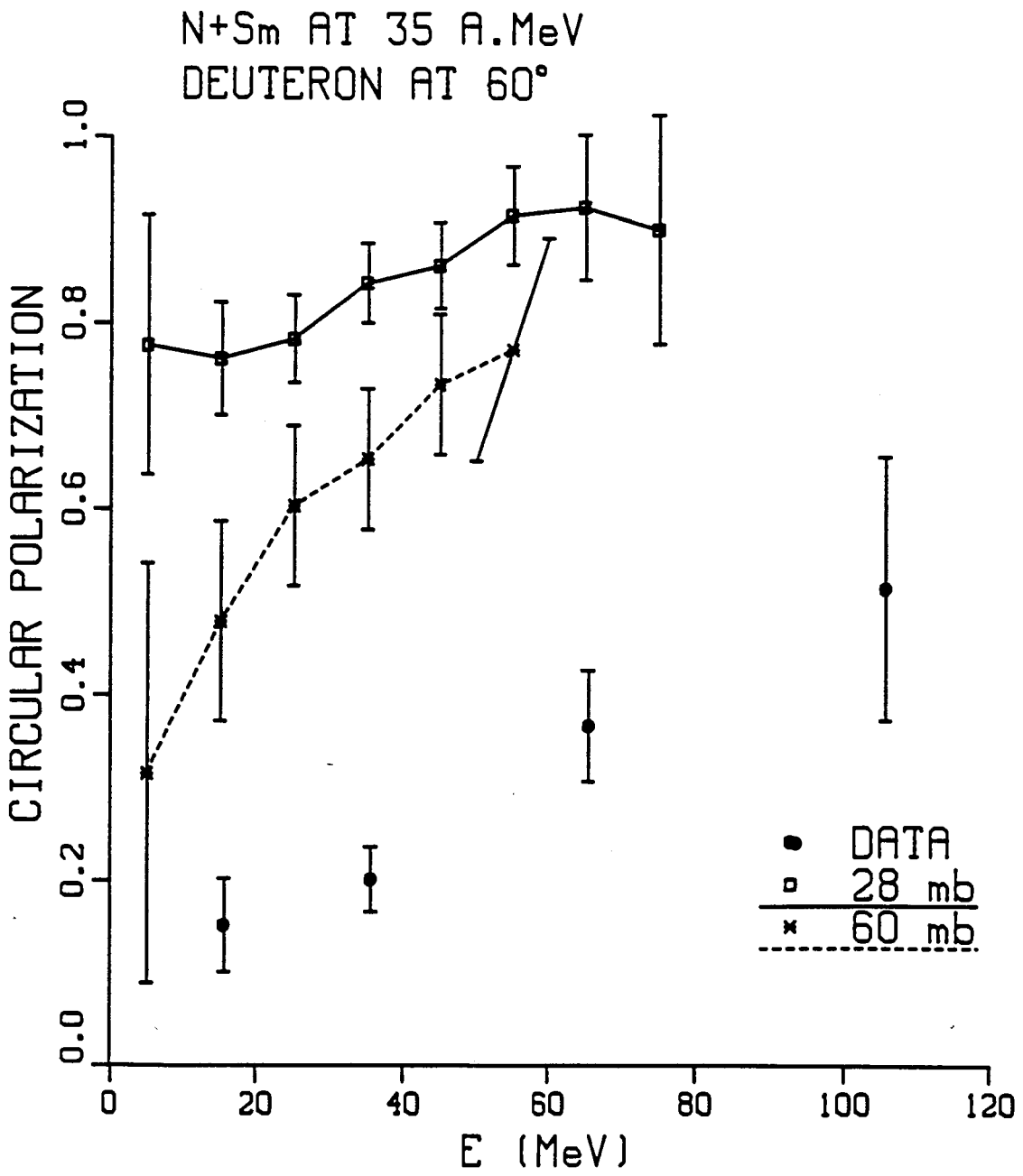

Fig. 4.8 Comparison of simulation and experiment for deuteron triggered events at 60°. Two values of σ_{NN} were used in the simulation: 28 and 60 mb. Data are from Ref. 19. Statistical error bars of simulation are included.

4.4 Comparison with BUU Calculations

Since the circular polarization experiment has been analyzed through the BUU model, it is worthwhile making a comparison between the QPD predictions and those obtained in a BUU calculation[19] of the same reaction. As we have mentioned in the last chapter, the BUU code separates the fast 'unbound' nucleons from the bound target-like nuclei. It cannot distinguish different species of fragments. The results calculated with the BUU simulation in Ref. 19 are energy integrated. In order to compare our results with those of the simulation in Ref. 19, we calculate the circular polarization associated with a single nucleon trigger averaged over trigger energy. The results of both QPD and BUU models are shown in Table 4.1. The results predicted by QPD are higher than those by the BUU model by about 50% for a similar σ_{NN}.

Model	σ_{NN} (mb)	θ	P
QPD	28	30°	0.38
"	60	"	0.24
BUU	41	"	0.18
QPD	28	60°	0.51
"	60	"	0.40
BUU	41	"	0.25

Table 4.1 Gamma ray circular polarization associated with nucleon triggers predicted by the QPD and BUU models. Results of the BUU model are taken from Ref. 19.

In order to illustrate the dependence of the predicted circular polarizations on the nucleon-nucleon collision dynamics, the BUU model[19] is used to calculate the circular polarizations using various nucleon-nucleon scattering cross sections at a fixed impact parameter b = 6.5 fm. The results are shown in Table 4.2. The predicted circular polarizations decrease for larger values of σ_{NN}. These results qualitatively agree with our results: the reactions with larger σ_{NN} give smaller circular polarizations.

σ_{NN} (mb)	P
0	0.82
10.3	0.56
20.5	0.24
41.0	0.25
82.0	0.04

Table 4.2 Circular polarization predicted[19] by the BUU model using different σ_{NN} at a fixed impact parameter of b = 6.5 fm. The nucleon trigger angle is 60°.

4.5 Microscopic Dynamics of the Collision Process

Let us now use the results of the computer simulations to examine the microscopic dynamics of the collision process. The simulation has predicted large values for the circular polarization of the gamma rays emitted. Thus, one expects that there is a strong correlation between

the trigger plane and the reaction plane. We begin our investigation of this question by examining the distributions of the impact parameters for a given trigger energy and angle. In this section, let us use the x and z axes of a Cartesian coordinate system to define the trigger plane: the z-axis is defined by the beam direction and the positive x-axis is the direction in which lies that component of the trigger momentum which is perpendicular to the beam. The impact parameter vector then lies in the x-y plane perpendicular to the beam.

A scatter plot (from the simulation) of the impact parameter for proton triggers at 30° with 28 mb for the in-medium NN cross section is plotted in Figure 4.9. The three sections of the plot correspond to proton kinetic energies of 20-30, 40-50 and 60-70 MeV respectively. Each dot on the plots represents the point where the beam intersects the x-y plane for one event. In other words, the impact parameter vector for each event is from the origin to the dot. In generating the scatter plots, we have shifted the magnitude (but not the direction) of the impact vector randomly up to ±0.5 fm. If the magnitudes are not shifted, the data points will fall in concentric circles because the impact parameters used in the simulation are taken to be 0.5, 1.5, ... , 7.5 fm in 1 fm steps. The shift of magnitude will give a more clear display of the density of points.

At low proton trigger energy, there is a very pronounced enhancement for impact parameters on the opposite side of the beam from the trigger momentum. There is a small enhancement on the same side as the trigger momentum. As one compares parts a) to c)

of Figure 4.9, one can see the tendency for the impact parameter to be located on the opposite side of the trigger momentum becoming stronger with trigger energy. The same behavior can be found in the scatter plots of the deuteron trigger. Figure 4.10 shows the deuteron trigger at kinetic energies of 20-30, 40-50, 60-70 and 80-90 MeV respectively. The conditions are same as those in Figure 4.9. We can conclude that the higher the trigger energy, the stronger the tendency to scatter to the opposite side of the impact parameter vector, i.e., the stronger the tendency of negative deflection.

For both trigger masses, the results of the simulation show that the path of the beam nucleus is bent around the target nucleus as the two nuclei interact. Some of the mass of the projectile is transferred to the target nucleus which gains angular momentum. The projectile nucleus usually does not "bounce off" the target, i.e. be positively deflected, at these trigger energies. This tendency is also what we have been led to expect from the circular polarization results.

To make a more quantitative argument, we evaluate the expectation value of the angle ϕ between the reaction plane and the trigger plane. For all the cases considered, $\bar{\phi}=\langle\phi\rangle$ is close to π, as one would expect. However, the average of randomly distributed angles on a plane is also π. To make sure the ϕ is not randomly distributed, we have evaluated the dispersion D of the angle ϕ where the dispersion D is defined as $\langle(\phi-\bar{\phi})^2\rangle^{1/2}$. For randomly distributed angles on a plane, the dispersion is equal to $\pi/\sqrt{3}$. The calculated relative dispersion $R = \frac{D}{\pi/\sqrt{3}}$, is observed to decrease with increasing trigger energy

and, correspondingly, with circular polarization. Figure 4.11 shows the behavior of the relative dispersion as a function of the circular polarization for proton and deuteron triggers at 30° and σ_{NN}=28 mb. This figure is constructed by evaluating the dispersion and the circular polarization for each energy bin in Figures 4.6 and 4.8.

For low values of the circular polarization, the relative dispersion tends towards unity, indicating a random distribution of impact parameters on the xy-plane. As the circular polarization increases, the width of the impact parameter distribution narrows and the relative dispersion tends to zero as the circular polarization approaches unity. This is what one would expect: the larger the circular polarization (i.e., the more the angular momentum vector of the residual nucleus is perpendicular to the reaction plane), the more the reaction and trigger planes are coincident. In other words, the simulation shows the circular polarization is a good indicator of the correlation between the reaction and trigger planes.

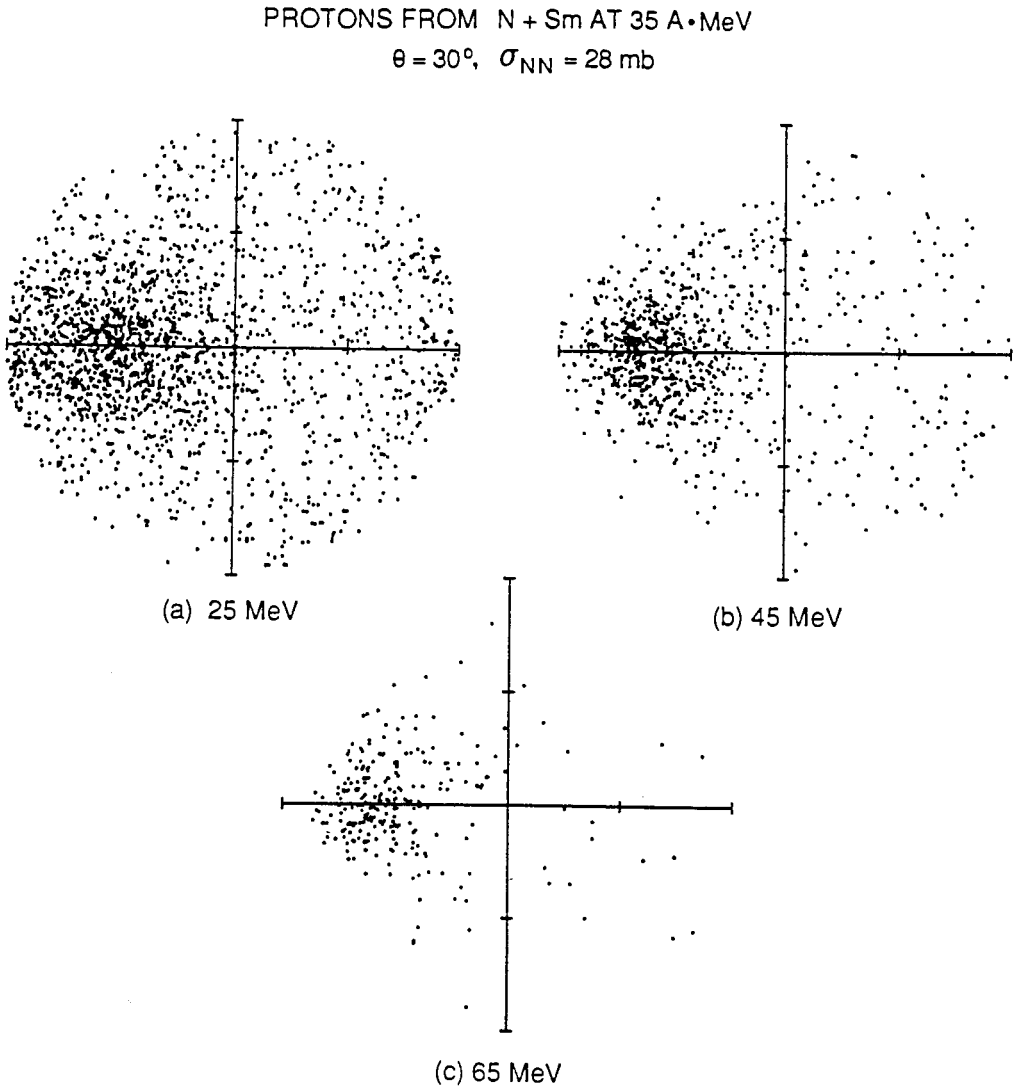

Fig. 4.9 Distribution of impact parameter **b** for proton triggers emitted at 30° and a range of energies. The acceptance range of each energy shown is ±5 MeV. Cross marks are placed on the axes every 4 fm.

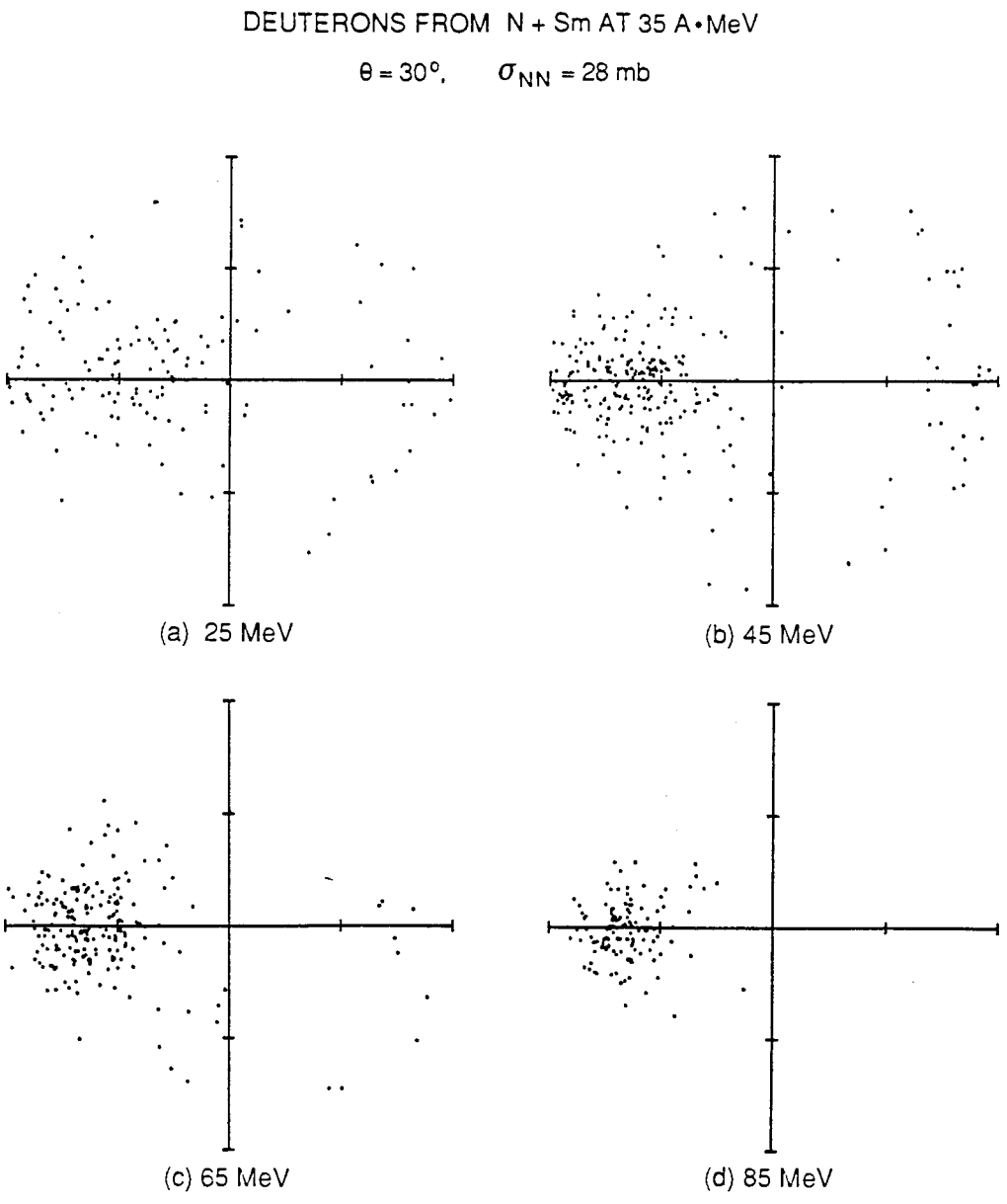

Fig. 4.10 Distribution of impact parameter **b** for deuteron triggers emitted at 30°.

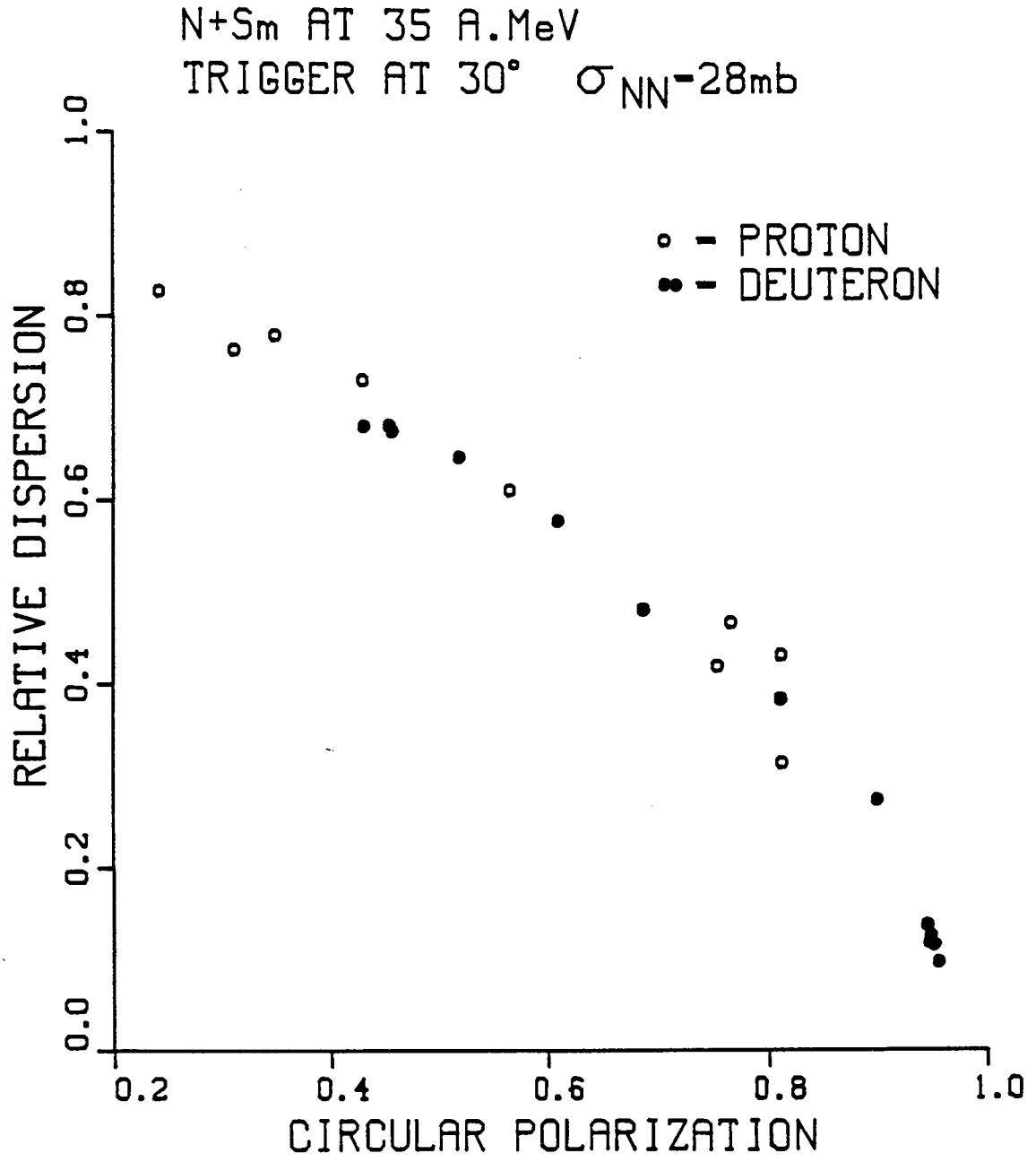

Fig. 4.11 Relative dispersion of the orientation of the reaction plane with respect to the trigger plane shown as a function of circular polarization for both values of σ_{NN} in the simulation.

Chapter Five

Conclusion

In this thesis, we perform a computer simulation based on the QPD model for the reaction of $^{14}N+^{154}Sm$ at 35 A.MeV. The single particle – proton, deuteron and triton – inclusive spectra and the gamma ray circular polarization in coincident with the light particle triggers are studied. The results are compared with the experimentally observed values and those calculated from the BUU model.

The difference between the data and the QPD are usually within three standard deviations for the inclusive spectra. The agreement is in the range expected. The difference between A value of 28 mb chosen for the in-medium NN cross section gives better agreement with the data compared to 60 mb, but a solid conclusion cannot be drawn because of the uncertainties which may arise from effects which are not incorporated in the model.

For example, the collision is only followed for a time of 250 fm/c which is long enough to ensure that the clusters are stabilized. The residual system is still highly excited. It takes a much longer time for the residues and other clusters to decay into their ground states by particle or gamma emission. Processes such as evaporation have a much longer time-scale than that for which it is practicable to run the simulation. Moreover, the QPD model does not include any decay via tunnelling through the potential barrier nor a mechanism for dealing with gamma decay. It is impossible for the QPD model to

predict long-time decay. Certainly, long-time-frame evaporation will boost the yields of light mass particles and might bring the σ_{NN}=60 mb predictions into better agreement with the data.

The nucleon spectra calculated from the QPD model have a similar shape to those found in a BUU calculation. The spectra from the BUU model are at a factor of two-three higher in magnitude than those from the QPD model. Given the different definition of the observable in the two models, the agreement is in the range expected.

The predicted circular polarizations are in qualitative agreement with the data in terms of trends with respect to fragment trigger, mass, energy and emission angle. However, the predictions by the QPD model are consistently higher than the data. Again, part of the reason for the discrepancy lies in long-time decays which will reduce the alignment of the angular momentum vector of the residual nucleus.

To see how large an effect this would be on the time scale of 1000 fm/c, we take a sample of the ^{163}Ho nuclei discussed in Chapter Three and propagate them for an extra 1000 fm/c. The change in orientation of the angular momentum vector is observed to be less than 1%. This demonstrates:

i) that there are few evaporative decays on a time frame which can be handled by the simulation, and

ii) that the simulation conserves angular momentum very well.

When a statistical decay code was used[24] to provide an estimate of the depolarization effects of evaporative decays, it was found that the predicted circular polarization could decrease by as much as 30%. This estimate significantly reduces the discrepancy between our predictions and the data, but does not eliminate it entirely. Lastly the assumption that the gamma decays are stretched E2 may be too strong. If other nonstretched transitions are considered, the circular polarization can be reduced by 20%.[25]

The circular polarizations calculated from the BUU model, which are about 50% of those predicted by the QPD model, seem to give better agreement with the data in comparison with the results of the QPD model. However, individual nucleon-nucleon scattering in the BUU model[19] that we are comparing with does not necessarily conserve angular momentum. (The observed angular momentum for the whole nuclear system is usually conserved). On the other hand, the angular momentum of nucleon-nucleon scattering and thus that of the whole nuclear system in the QPD model is conserved. Since the conservation of angular momentum is a very important factor in the determination of the gamma ray circular polarization, we cannot agree that the BUU model gives better prediction than the QPD does.

The central question which we ask of the simulation is whether there is a strong correlation between the circular polarization and the distribution of the reaction plane's orientation with respect to the trigger plane. The simulation finds that the angle between the two planes is about 180° and the dispersion of the angle decreases as the

circular polarization increases. Therefore, it shows that there is indeed a correlation, and that the correlation becomes stronger the closer the circular polarization is to unity. Further the impact parameter tends to point in the opposite direction to the trigger direction. This indicates that the long range nuclear interaction tends to pull the nuclei around one another, although not sufficiently strongly as to result in an orbiting pair at these bombarding energies.

References:

1 Bertsch, G.F., and S. Das Gupta, Physics Reports **160**, 189 (1988).

2 Gelbke, C.K., and D.H. Boal, Prog. Part. Nucl. Phys. **19**, 33 (1987).

3 Stöcker, H., and W. Greiner, Physics Reports **137**, 277 (1986).

4 Boal, D.H., Ann. Rev. Nucl. Part. Sci. **37**, 1 (1987).

5 Kikuchi, K., and M. Kawai, *Nuclear Matter and Nuclear Reaction* . (North-Holland: Amsterdam, 1968).

6 Nix, J.R., *et al*, Phys. Rev. C**25**, 2491 (1982).

7 Cugnon, J., *Lecture given at Cargese Summer School* (1984).

8 Bertsch, G., and J. Cugnon, Phys. Rev. C**24**, 2514 (1981).

9 Balescu, R., *Equilibrium and Nonequilibrium Statistical Mechanics.* (Wiley: New York, 1975).

10 Nordheim, L.W., Proc. R. Soc. London, Ser. A **119**, 689 (1928).

11 Uehling, E.A., and G.E. Uhlenbeck, Phys. Rev. **43**, 552 (1933).

12 Binder, K., *Application of the Monte Carlo Method in Statistical Physics.* (Springer-Verlag: New York, 1987).

13 Gan, H.H., S.J. Lee and S. Das Gupta, Phys. Rev. C**36**, 2365 (1987).

14 Aichelin, J., and G. Bertsch, Phys. Rev. C**31**, 1730 (1985).

15 Kruse, H., *et al*, Phys. Rev. C**31**, 1770 (1985).

16 For example, see C. Gale and S. Das Gupta, Phys. Lett. **162**B, 35 (1985); G.E. Beauvais *et al*, Phys. Rev. C**35**, 545 (1987); J. Aichelin and H. Stocker, Phys. Lett. **176**B, 14 (1986).

17 Boal, D.H., and J.N. Glosli, Phys. Rev. C**38**, 1870 (1988); and Phys. Rev. C**38**, 2621 (1988).

18 Tsang, M.B., *et al.*, Phys. Rev. Lett. **52**, 1967 (1984).

19 Tsang, M.B., *et al.*, Phys. Rev. Lett. **57**, 559 (1986).

20 Trautmann, W., *et al.*, Phys Rev. Lett. **53**, 1630 (1984).

21 Bertsch, G.F., H. Kruse and S. Das Gupta, Phys. Rev. C **29**, 673 (1984).

22 Tsang, M.B., *et al.*, Michigan State University Preprint: MSUCL-681.

23 Boal, D.H., private communication.

24 Trautmann, W., *et al.*, Nucl. Instrum. Methods **184**, 449 (1981).

25 Trautmann, W., *et al.*, Nucl. Phys. **A422**, 418 (1984).